Check for updates

JGR Oceans

RESEARCH ARTICLE

10.1029/2025JC022414

Biogeochemical Implication of Massive Episodic Flood Deposition: Model-Data Integration

Stanley Nmor[1,2], Eric Viollier[1], Lucie Pastor[3], Bruno Lansard[1], and Christophe Rabouille[1]

[1]Laboratoire des Sciences du Climat et de l'Environnement, LSCE/IPSL, CEA-CNRS-UVSQ-Université Paris Saclay, Gif sur Yvette, France, [2]Department of Estuarine and Delta Systems, Royal Netherlands Institute of Sea Research (NIOZ), Yerseke, The Netherlands, [3]ABF Décisions, Bordeaux, France

Key Points:

- The study focuses on two different flood depositions (30 cm poor vs. 10 cm rich in organic carbon), with distinct biogeochemical responses
- The two different types of flood input drive contrasting evolutions of DIC flux and in general, enhance sediment metal cycling
- Consecutive flood deposition might disproportionately affect sulfate reduction and methanogenesis in coastal sediment

Correspondence to:

S. Nmor and C. Rabouille,
stanley.nmor@nioz.nl;
christophe.rabouille@lsce.ipsl.fr

Citation:

Nmor, S., Viollier, E., Pastor, L., Lansard, B., & Rabouille, C. (2025). Biogeochemical implication of massive episodic flood deposition: Model-data integration. *Journal of Geophysical Research: Oceans*, *130*, e2025JC022414. https://doi.org/10.1029/2025JC022414

Received 30 JAN 2025
Accepted 3 JUN 2025

Author Contributions:

Conceptualization: Stanley Nmor, Eric Viollier, Christophe Rabouille
Data curation: Lucie Pastor, Bruno Lansard, Christophe Rabouille
Formal analysis: Stanley Nmor, Eric Viollier, Bruno Lansard, Christophe Rabouille
Funding acquisition: Eric Viollier, Christophe Rabouille
Investigation: Stanley Nmor, Eric Viollier, Christophe Rabouille
Methodology: Stanley Nmor, Eric Viollier, Christophe Rabouille
Project administration: Eric Viollier, Christophe Rabouille
Resources: Eric Viollier, Christophe Rabouille
Software: Stanley Nmor

© 2025. The Author(s).
This is an open access article under the terms of the Creative Commons Attribution-NonCommercial-NoDerivs License, which permits use and distribution in any medium, provided the original work is properly cited, the use is non-commercial and no modifications or adaptations are made.

Abstract During extreme flood events, coastal deltas experience large sediment deposition within a short time period. The biogeochemical consequences of these deposition-recycling-burial processes on carbon and nutrient cycles are not fully understood. Using a coupled data model approach, we explore the early diagenetic responses of deltaic sediments influenced by two intense floods (in spring and fall) on the Rhône River in 2008. The data set shows that sediment porewater composition responded abruptly to this almost instantaneous change in deposition. The model calculated that these flood-related depositions increased organic carbon mineralization by a factor of 2–4 compared to preflood levels, and were dominated by sulfate reduction (68%), and methanogenesis (16%). The two floods (organic-poor in spring and organic-rich in fall) cause different diagenetic effects in terms of dissolved inorganic carbon (DIC) fluxes—the 30-cm organic-poor flood deposition induced a large storage of DIC in porewaters, which largely decreased its flux to the water column, whereas the 10-cm organic-rich sediment induced a large efflux of DIC. The model reveals the absence of dissolved sulfide in porewaters after flood deposition due to iron bound precipitation. The sequential flood depositions caused a temporary memory effect (i.e., interaction between two successive floods), with stronger effect for methane (38%), whose longer relaxation timescale limits complete recovery before the next event separated by 6 months. Increasing the frequency and intensity of these events in the future could lead to memory accumulation of flood biogeochemical signatures.

Plain Language Summary Coastal sediments are important for their role in the global carbon cycle as long-term sink of carbon. River deltas are major depositional sites of sediment, receiving large amounts of sediment, particularly during periods of heavy flooding. These flood depositions can trigger biogeochemical changes in the sediment. However, our understanding of the magnitude of the sediment response induced by these events is still poorly known. To answer this question, numerical model and data sets from two floods in 2008 driven by discharges from the Rhône River were used to investigate the size of the biogeochemical response following these events. Our findings suggest that these floods could cause differing responses, largely driven by the nature of the deposited flood layer. Using the model, we found a 2–4 times increase in overall bacterial recycling rates from preflood conditions, which resulted in different responses of dissolved inorganic carbon (DIC) exchange of the sediment with seawater. In the event of sequential flood deposition, cumulative biogeochemical changes can also occur and may affect the recovery of sediment after the flood. These effects might be more consequential if these intense floods continue to increase due to climate change.

1. Introduction

River-dominated ocean margins (RiOMar) are important for connecting the terrestrial and marine organic carbon cycles (OC) (Mackenzie et al., 2004; Regnier et al., 2022) by filtering the transfer of material from the river systems on continental margins to the open ocean. They also serve as a major organic matter (OM) deposition center, which has implications for preservation and burial. Indeed, continental margins account for more than 85% of all organic carbon burial in the ocean (Tegler et al., 2024), with deltas (RiOMars) representing half of the shelf burial (Burdige, 2005). At the same time, river deltas are active biogeochemical reactors that emit large quantities of CO_2 to the atmosphere (Cai, 2011; Dai et al., 2022).

These RiOMar systems are also vulnerable to extreme flood events, which are known to transport large amounts of sediment, carbon, and nutrients from the land to the oceans, with their primary depositional zone occurring preferentially in the connecting deltas (McKee et al., 2004). Massive sediment inputs driven by these flood events

Supervision: Eric Viollier, Bruno Lansard, Christophe Rabouille
Validation: Stanley Nmor, Eric Viollier, Lucie Pastor, Bruno Lansard
Visualization: Stanley Nmor
Writing – original draft: Stanley Nmor, Eric Viollier, Christophe Rabouille
Writing – review & editing: Stanley Nmor, Eric Viollier, Lucie Pastor, Bruno Lansard, Christophe Rabouille

have been observed in many deltaic systems, for example, Amazon River (Aller et al., 1996; Montanher et al., 2018), Mississippi River (Morse & Rowe, 1999), Atchafalaya River (Allison et al., 2000), Eel River (Bentley & Nittrouer, 2003), Po River (Palinkas et al., 2005; Tesi et al., 2012, 2013), Têt River (Bourrin et al., 2008), Rhône River (Cathalot et al., 2010). These large transfers of sediment are projected to occur with increasing frequency due to changing environmental landscapes and climate change (Tockner & Stanford, 2002). Indeed, the current trend in extreme precipitation from hurricanes and other storm events can result in large amounts of sediment being delivered in a short period of time, as documented in some coastal margins: Tropical Storm Lee transported sediment to a large portion of Cheapeake Bay via the Susquehanna River (Cheng et al., 2013), extreme precipitation events in the Mississippi River basin transferred large volume of terrestrial organic carbon to the northern Gulf of Mexico (Bianucci et al., 2018), large quantities of sediment were transported on the northeastern Australian coast during Cyclone Winifred (Carter et al., 2009), to name a few. All of these events have been shown to have a short (daily)-to-medium (yearly) impact on the ecosystem productivity, such as degrading water clarity and growth of phytoplankton (Cheng et al., 2013), increasing OM mineralization in bottom waters of the coastal ocean inducing hypoxic condition (Cheng et al., 2013; Moriarty et al., 2021), or increased CO_2 flux to the atmosphere (Osburn et al., 2019).

In the Gulf of Lions (the southern part of France), about 80% of the annual terrigenous particulate input is delivered by Rhône River floods (Antonelli et al., 2008) with a large majority of the materials deposited in the prodeltaic zone (Estournel et al., 2023; Ulses et al., 2008). The terrestrial input is dominant at the station investigated in the Rhône prodelta near the river mouth (station A in Wu et al. (2018)). The deposition of riverine material carrying ^{7}Be is clearly visible with large inventories down to 15 cm for the two recorded events (June and December 2008), which indicates intense deposition of sediment and carbon at the 20-m deep stations. The sediment delivered by these flood events can differ in terms of its quantity and organic matter quality/reactivity, as they represent a conglomeration of different particles originating from different regions of the catchment (Eyrolle et al., 2012; Pont et al., 2017). In addition, given the unique sedimentary characteristics of the prodelta (high sedimentation up to 40 cm yr^{-1}—Charmasson et al. (1998) and high carbon flux up to 54 mol C $m^{-2}yr^{-1}$—Pastor et al. (2011b)), the underlying diagenetic sequence of sediment shows remarkable stationarity during spring and summer (high concentration of DIC), dissolved iron and manganese, and strong sulfate reduction (Rassmann et al. (2020)), despite short-term biogeochemical response of oxygen linked to fall and spring floods (Cathalot et al., 2010). The reason for such long-term stability yet short-term response is still unknown (Pastor et al., 2018); however, it has been linked to the system's shorter relaxation timescale (4–5 months) (Nmor et al., 2022). In the context of a changing climate and increasing frequency and intensity of extreme events such as floods, the central question is as follows: *Does increasing frequency and magnitude of flood deposition influence the biogeochemical functioning of coastal sediments?*

While a proper understanding of the characteristics of this type of perturbation would require continuous monitoring and observation, both on a long and short term (Ferreira et al., 2024; Toussaint et al., 2014), there is still a scarcity of data on the estimated biogeochemical fluxes and rates caused by these flood events. Combination of available data (Bonifácio et al., 2014; Bourgeois et al., 2011; Cathalot et al., 2010; Pastor et al., 2018), with appropriate spatiotemporal scale, and numerical modeling can thus help to answer some of these questions.

This study aims at quantifying the size and scope of biogeochemical changes induced by significant flood events in the Rhône prodelta region. A reaction-transport model with a nonsteady state approach was used to investigate how the diagenetic mineralization of organic matter can explain porewater data obtained from observations of two distinct flood deposition events in 2008. We also calculated the biogeochemical fluxes and rates associated with these events, as well as the system's temporal evolution after this perturbation. The effect of these flood events on carbon, iron, manganese, and sulfur cycling was then determined. The results of this model-data investigation provides new insights into the consequences of these extreme events on sediment biogeochemical dynamics.

2. Materials and Methods

2.1. Data Description

The data set discussed in this paper covers the major flood deposition events, which occurred in the Rhône prodelta in the year 2008 (Cathalot et al., 2010; Pastor et al., 2018). The data described the hydro-

21699291, 2025, 6, Downloaded from https://agupubs.onlinelibrary.wiley.com/doi/10.1029/2025JC022414 by Universitetsbiblioteket, Wiley Online Library on [07/01/2026]. See the Terms and Conditions (https://onlinelibrary.wiley.com/terms-and-conditions) on Wiley Online Library for rules of use; OA articles are governed by the applicable Creative Commons License

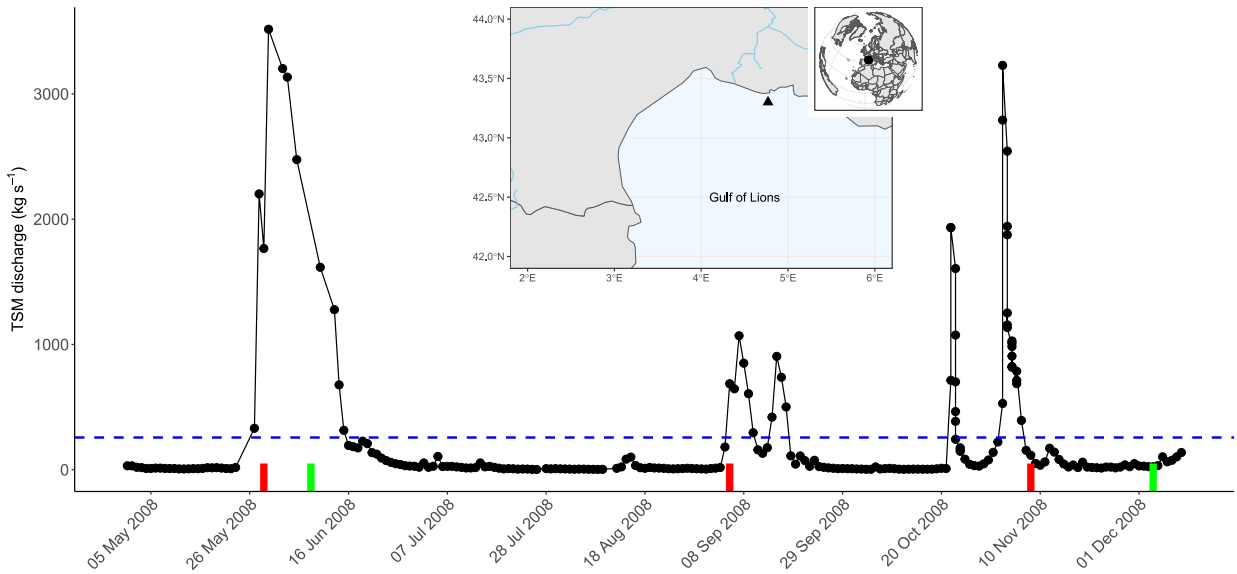

Figure 1. Time series of total suspended matter (TSM) river discharge by the Rhône River in year 2008. The red bar denotes the day of deposition used in the model, and the green bar is the sampling date when measurement was carried out. The blue dashed line is the annual mean of TSM discharge. Data were obtained from the Mediterranean Oceanic Observing System for the Environment (MOOSE database) provided by Mediterranean Institute of Oceanology. Insert: a map of the Gulf of Lions showing the location of the station where the data used in this study was collected.

sedimentological and chemical situation of the prodelta sediment within 2 km from the river mouth (Station A: 4° 51.099°E and 43°18.751°N). The average depth at this location is 23 m (Pastor et al., 2018) with high apparent accumulation rates up to 40 cm yr^{-1} (Charmasson et al., 1998). It is worth noting that these proximal stations in the Rhône prodelta are typical of sediments with large organic carbon inputs, which lead to large anoxic diagenesis (Rassmann et al., 2016). These intense anoxic processes associated with large sedimentation rates produce significant FeS precipitation and burial (Rassmann et al., 2020). This decouples the diffusive oxygen flux from the DIC flux, therefore generating a DIC/O_2 flux ratio in the range of 2–7.

The present paper deals with the flood events of May/June 2008 (generalized flood) and November/December 2008 (Cenevol flood). Full description of the data set can be found in Cathalot et al. (2010) and Pastor et al. (2018). The May/June generalized flood is referred to as the spring flood, whereas the November/December cenevol flood is referred to as the fall flood. The sampling dates are specified in Figure 1. In the spring flood, 30 cm of sediment was deposited. The average organic carbon content in this layer of sediment (1% d.w.) was lower than the average OC in preflood sediment (>2% d.w.; Cathalot et al. (2010)), with deposited materials primarily composed of aggregated siliceous and carbonate crystalline rocks from nearby tributaries (Durance and Isère Rivers) containing large amounts of refractory carbon (Cathalot et al., 2013; Copard et al., 2018). During the fall flood, a sediment layer of 10 cm thickness was deposited mostly composed of silicate minerals and organic debris with a high OC content (5% d.w.; Cathalot et al. (2010)) and a large amount of young OC (Cathalot et al., 2013). Porewater composition including dissolved iron (Fe^{2+}) and manganese (Mn^{2+}) profiles in both events showed evidence of this flood perturbation, with these species responding sequentially to the deposition (Pastor et al., 2018). This response was characterized by a slow buildup of iron following manganese release in the first 30 cm of porewater. Furthermore, significant sulfate reduction was observed within the sediment, with sulfide concentrations below the detection limit (<0.5 μM).

2.2. Model Description

The model used for this study is the time-dependent, one-dimensional reactive transport model, FESDIA (Nmor et al., 2022). This model described the transformation of OC within the sediment column with well-adapted capabilities for usage in sudden flood depositional scenarios. The full description of the model, detailed mass

21699291, 2025, 6, Downloaded from https://agupubs.onlinelibrary.wiley.com/doi/10.1029/2025JC022414 by Universitetsbiblioteket, Wiley Online Library on [07/01/2026]. See the Terms and Conditions (https://onlinelibrary.wiley.com/terms-and-conditions) on Wiley Online Library for rules of use; OA articles are governed by the applicable Creative Commons License

21699291, 2025, 6, Downloaded from https://agupubs.onlinelibrary.wiley.com/doi/10.1029/2025JC022414 by Universiteitsbibliotheek, Wiley Online Library on [07/01/2026]. See the Terms and Conditions (https://onlinelibrary.wiley.com/terms-and-conditions) on Wiley Online Library for rules of use; OA articles are governed by the applicable Creative Commons License

Table 1
State Variables Described in the Model

State variable	Description	Model notation	Units
C_{org}^{fast}	Fast decaying detritus	FDET	mmol C m^{-3} solid
C_{org}^{slow}	Slow decaying detritus	SDET	mmol C m^{-3} solid
$FeOOH_A$	Fast oxidized ferric iron	FeOOHA	mmol Fe m^{-3} solid
$FeOOH_B$	Slow oxidized ferric iron	FeOOHB	mmol Fe m^{-3} solid
MnO_{2A}	Fast oxidized manganese	MnO2A	mmol Mn m^{-3} solid
MnO_{2B}	Slow oxidized manganese	MnO2B	mmol Mn m^{-3} solid
O_2	Oxygen	O2	mmol O_2 m^{-3} liquid
NO_3^-	Nitrate	NO3	mmol N m^{-3} liquid
NH_4^+	Ammonium	NH3	mmol N m^{-3} liquid
SO_4^{2-}	Sulfate	SO4	mmol S m^{-3} liquid
H_2S	Hydrogen sulfide	H2S	mmol S m^{-3} liquid
Fe^{2+}	Reduced ferrous iron	Fe	mmol Fe m^{-3} liquid
Mn^{2+}	Reduced manganese	Mn	mmol Mn m^{-3} liquid
DIC	Dissolved inorganic carbon	DIC	mmol C m^{-3} liquid
CH_4	Methane	CH4	mmol CH4 m^{-3}liquid
$MnCO_3$	Mn carbonate	MnCO3	mmol Mn m^{-3} solid
S^0	Elemental sulfur	S0	mmol S m^{-3} liquid
FeS	Iron monosulfide	FeS	mmol S m^{-3} solid
FeS_2	Pyrite	FeS2	mmol S m^{-3} solid

balance equations, and reaction kinetics can be found in Nmor et al. (2022). Here, we recap the key biogeochemical reactions and pathways necessary to simulate the flood data sets derived from Pastor et al. (2018).

The reactive transport model includes 9 solid phase state variables—fast (C_{org}^{fast}) and slow C_{org}^{slow} degradable organic matter, two pools of manganese oxide (MnO_{2A} and MnO_{2B}) and iron hydroxide ($FeOOH_A$ and $FeOOH_B$), authigenic sulfide bounded iron mineral (iron monosulfide (FeS)), stable pyrite (FeS_2), and manganese carbonate ($MnCO_3$) (Table 1). The choice of iron and manganese fractions was dictated by the assumption that the short-term path of Fe and Mn dynamics is driven by the reactive pool of their respective oxides (Thamdrup, 2000). In practice, the iron oxide pool broadly consists of highly reactive (amorphous and crystalline) oxides— ferrihydrite, goethite, lepidocrocite, and hematite) with half-lives of <1 year (Canfield et al., 1992; Raiswell & Canfield, 1998), moderately reactive component (magnetite and reactive silicate of half-life of 10^2 year), and poorly reactive iron oxide with longer half-life, $>10^5$ year (Canfield et al., 1992; Poulton et al., 2004). Detrital iron fraction bound within sheet silicates is nonreactive on the timescale of early diagenetic processes of concern to the model (Poulton & Raiswell, 2002). The particulate iron bonded to sulfide (FeS formed via precipitation leads to the buildup of FeS_2) has great stability and poor solubility, and hence can be assumed to remain permanently buried (see below and Rassmann et al. (2020)). Similarly, manganese oxides or (oxyhydroxides) in the sediment span different reaction timescales, and only the reactive fractions were considered in the model. Our modeling strategy is analogous to other diagenetic models that describe metal cycling in marine sediment (Berg et al., 2003; Dale et al., 2015; van de Velde et al., 2018; Zhao et al., 2020).

Dissolved species included in the model are oxygen (O_2), nitrate (NO_3), ammonium (NH_4^+), dissolved iron (Fe^{2+}) and manganese (Mn^{2+}), sulfate (SO_4^{2-}), hydrogen sulfide (H_2S), methane (CH_4), dissolved inorganic carbon (DIC), and intermediate elemental sulfur (S^0) (Table 1).

21699291, 2025, 6, Downloaded from https://agupubs.onlinelibrary.wiley.com/doi/10.1029/2025JC022414 by Universitetsbiblioteket, Wiley Online Library on [07/01/2026]. See the Terms and Conditions (https://onlinelibrary.wiley.com/terms-and-conditions) on Wiley Online Library for rules of use; OA articles are governed by the applicable Creative Commons License

Degradation of organic matter (OM) occurs via the sequence of energy utilization of electron acceptors (Froelich et al., 1979), with oxygen used first, followed by oxidation via NO_3. Thereafter, the model includes microbial-mediated reduction of oxides of Mn and Fe (MnO_2 and $FeOOH_3$) justified by the substantial release of their respective reduced solutes during flood deposition (Pastor et al., 2018). Sulfate reduction and methanogenesis close the carbon-based cycle of OM remineralization in the model (Equation 1).

$$\begin{aligned}
&\mathrm{OM} + \mathrm{O_2} \rightarrow \mathrm{CO_2} + \frac{1}{(\mathrm{C:N})}\mathrm{NH_3} + \mathrm{H_2O} \\
&\mathrm{OM} + 0.8\mathrm{NO_3^-} + 0.8\mathrm{H^+} \rightarrow \mathrm{CO_2} + \frac{1}{(\mathrm{C:N})}\mathrm{NH_3} + 0.4\mathrm{N_2} + 1.4\mathrm{H_2O} \\
&\mathrm{OM} + 2\mathrm{MnO_{2A}} + 4\mathrm{H^+} \rightarrow \mathrm{CO_2} + \frac{1}{(\mathrm{C:N})}\mathrm{NH_3} + 2\mathrm{Mn^{2+}} + 3\mathrm{H_2O} \\
&\mathrm{OM} + 4\mathrm{FeOOH} + 8\mathrm{H^+} \rightarrow \mathrm{CO_2} + \frac{1}{(\mathrm{C:N})}\mathrm{NH_3} + 4\mathrm{Fe^{2+}} + 7\mathrm{H_2O} \\
&\mathrm{OM} + 0.5\mathrm{SO_4^{2-}} + \mathrm{H^+} \rightarrow \mathrm{CO_2} + \frac{1}{(\mathrm{C:N})}\mathrm{NH_3} + 0.5\mathrm{H_2S} + \mathrm{H_2O} \\
&\mathrm{OM} \rightarrow 0.5\mathrm{CO_2} + \frac{1}{(\mathrm{C:N})}\mathrm{NH_3} + 0.5\mathrm{CH_4}
\end{aligned} \tag{1}$$

where OM is simply represented as $((CH_2O)(NH_3)_{N:C})$ and N:C is the Redfield nitrogen to carbon ratio (N:C = $\frac{16}{106}$). The reactive rates are represented by Michaelis-Menten type relationships with respect to the oxidant concentrations.

The direct consequence of organic matter remineralization in the model is the production of reduced substances (Equation 1). The model considers a series of subsequent processes connected to these reduced species (Equation 2). In order to reduce the degree of freedom for calibrating poorly constrained parameters and processes, which govern many of the secondary reactions in the Rhône prodelta sediment, simplified representations of the iron, manganese, and sulfur interactions were made.

Reoxidation of reduced species from OM mineralization via oxygen (Equation 2) and metallic oxides (Equation 2) is included while methane formed by fermentation of OM can be anaerobically oxidized (i.e., anaerobic oxidation of methane, AOM) (Dale et al., 2006). Fe^{2+} is oxidized to ferric iron (Fe^{3+}), which precipitates out as fresh iron oxide ($FeOOH_A$) minerals. Sulfide produced by sulfate reduction can be abiotically oxidized by both pools of iron oxyhydroxydes and manganese oxides (i.e., sulfur-mediated iron and manganese reduction) (Berg et al., 2003). As discussed in Burdige (1993) and Haese (2000), the interaction between dissolved Fe^{2+} and H_2S happens in two stages, with the formation of intermediate dissolved elemental sulfur (S^0) and dissolved FeS (FeS_{aq}). These forms of sulfur are modeled in a sequential fashion and because of their relatively unstable state in marine sediment, they can coprecipitate into its particulate form (FeS_p) once a solubility threshold of ~2 μM is reached (Rickard, 2006). Therefore, we assumed that dissolved FeS, upon formation, is subsequently transformed into a stable form of particulate sulfur that can be eliminated from the porewaters via precipitation (Rickard, 1997, 2006). The kinetic rate expressions of all reoxidation processes and other secondary reactions are described by standard second-order rate formulation.

The model also includes a simple representation of the formation and dissolution of manganese carbonates (Rhodocrosite). However, the formation and dissolution of iron carbonate, known as siderite, were not included in the model. This is because they play a small role in the redox cycling of iron in marine sediments (Haese, 2000). This kinetics of dissolution and precipitation follow a similar formulation in Wang and Van Cappellen (1996), where the reaction rates are dependent on the porewater saturation state. Here, the pH of the porewater was not explicitly modeled but was fixed at a constant value of 7.5 in order to reduce the complexity of the model (Berg et al., 2003; van de Velde & Meysman, 2016).

21699291, 2025, 6, Downloaded from https://agupubs.onlinelibrary.wiley.com/doi/10.1029/2025JC022414 by Universitetsbiblioteket, Wiley Online Library on [07/01/2026]. See the Terms and Conditions (https://onlinelibrary.wiley.com/terms-and-conditions) on Wiley Online Library for rules of use; OA articles are governed by the applicable Creative Commons License

$$
\begin{aligned}
NH_4^+ + 2O_2 &\rightarrow NO_3^- + H_2O + 2H^+ \\
2Mn^{2+} + O_2 + 2H_2O &\rightarrow 2MnO_{2A} + 4H^+ \\
4Fe^{2+} + O_2 + 6H_2O &\rightarrow 4FeOOH_A + 8H^+ \\
H_2S + 2O_2 &\rightarrow SO_4^{2-} + 2H^+ \\
CH_4 + 2O_2 &\rightarrow CO_2 + 2H_2O \\
2Fe^{2+} + MnO_{2A/B} + 2H_2O &\rightarrow 2FeOOH_A + Mn^{2+} + 2H^+ \\
H_2S + MnO_{2A/B} + 2H^+ &\rightarrow S^0 + Mn^{2+} + 2H_2O \\
H_2S + 2FeOOH_{A/B} + 4H^+ &\rightarrow S^0 + 2Fe^{2+} + 4H_2O \\
CH_4 + SO_4^{2-} &\rightarrow HCO_3^- + HS^- + H_2O \\
Fe^{2+} + H_2S &\rightarrow FeS + 2H^+ \\
Mn^{2+} + HCO_3^- &\leftrightarrow MnCO_3 + H^+ \\
FeS + S^0 &\rightarrow FeS_2 \\
FeS + 2O_2 &\rightarrow Fe^{2+} + SO_4^{2-}
\end{aligned}
\tag{2}
$$

2.3. Model Parameters

The key rate parameters for the biogeochemical processes are tabulated in Table 2. The environmental parameters and boundary conditions were derived from previous steady-state modeling studies investigated in the Rhône prodelta sediment (Ait Ballagh et al., 2021; Pastor et al., 2011c). For our model-data calibration, parameters associated with the transport processes (advection, irrigation, and bioturbation) were first adjusted before pathways involving the carbon dynamics were fine-tuned (I and C in Table 2).

The carbon-based parameters were specified with respect to range of values reported in the aforementioned studies with little modification (M in Table 2). Thus, for the processes associated with OM mineralization, our model fitting procedure was constrained by these prior best fits (Ait Ballagh et al., 2021; Pastor et al., 2011c). Thereafter, the processes affecting the iron and manganese cycles were then parameterized. As these previous diagenetic modeling studies only capture the anaerobic processes by considering a lumped term, ODU (oxygen demand unit), nominal additional parameters pertaining to the coupled iron-sulfur-manganese cycle were derived from other published works (C in Table 2) (Berg et al., 2003; Dale et al., 2015; Wang & Van Cappellen, 1996; Zhao et al., 2020).

However, because the boundary flux for other particulate species besides carbon in the Rhône prodelta sediments is largely unknown, the parameters involving sulfur, iron, and manganese interactions were fine-tuned to the data at hand using both manual and automatic fitting procedures provided by the R package FME (Soetaert & Petzoldt, 2010), while accounting for physical/biogeochemical constraints intrinsic to the study site (e.g., low sulfide system; <2 μM (Pastor et al., 2018)), high sedimentation rate and carbon flux; 10–40 cm y^{-1} (Pastor et al., 2011c), low bioturbation; 0.05 cm^2 d^{-1} (Pruski et al., 2015), and possibly high iron flux; ∼53,300 t (Marin & Giresse, 2001; Roussiez et al., 2011). The boundary condition for dissolved species (e.g., oxygen, sulfate, and DIC) are directly inferred from the observed data (O in Table 2).

2.4. Modeling Flood Deposition and Sediment Biogeochemical Dynamics

As introduced in Nmor et al. (2022), the diagenetic dynamics of the flood deposition events is driven by the characteristics of the sediment delivered (such as the deposit thickness, organic carbon content, and reactivity). In that study, the mechanism of flood-induced sediment deposition was modeled as a single massive event against an underlying background variation. However, in this paper, this singular flood prescription is expanded to include multiple events in one simulation run, thereby allowing a chain of event-driven simulation to be performed with their respective characteristics. As a consequence, the enrichment factor (α), which is the ratio of organic carbon (OC) in the new layer (TOC_{zpert}) compared to the layer below (TOC_{old}), becomes a value that changes over time. Its value depends on how thick the new deposit layer is and how much reactive carbon it contains. As the layer

Table 2
Summary of Parameters Used in the FESDIA Model

Description	Model name	Parameters	Units	Type	Source
Total organic C deposition	Cflux	10,000	nmol C cm^{-2} d^{-1}	I	1
Part FDET in carbon flux	pFast	0.2	–	C	1
Deposition rate of FeOOH	FeOH3flux	5,000	nmol Fe cm^{-2} d^{-1}	M	–
Flux of MnO2	MnO2flux	1,000	nmol Mn cm^{-2} d^{-1}	M	1
Decay rate FDET	rFast	0.03	d^{-1}	C	1
Decay rate SDET	rSlow	0.0031	d^{-1}	C	2
NC ratio FDET	NCrFdet	0.14	molN/molC	I	2
NC ratio SDET	NCrSdet	0.1	molN/molC	I	–
Oxygen	O2bw	238	µM	O	–
Nitrate	NO3bw	0	µM	O	–
Ammonium	NH3bw	0	µM	O	–
Methane	CH4bw	0	µM	O	–
DIC	DICbw	2	mM	O	–
Dissolved iron	Febw	0	µM	O	–
Hydrogen sulfide	H2Sbw	0	µM	O	–
Sulfate	SO4bw	30	mM	O	–
Manganese	Mnbw	0	µM	O	–
Advection rate	w	0.027	cm d^{-1}	M	1
Bioturbation coefficient	biot	0.05	cm^2 d^{-1}	C	3
Depth of mixed layer	biotdepth	5	cm	I	3
Attenuation coefficient below depth of mixed layer	biotatt	1	cm	I	–
Bio-irrigation rate	irr	0.3	d^{-1}	M	3
Depth of irrigated layer	irrdepth	7	cm	I	3
Attenuation coeff below irrdepth	irratt	1	cm	I	–
Max nitrification rate step1 (NH3ox)	rnitri	100	d^{-1}	M	–
Temperature	temperature	15.6	dgC	M	–
Salinity	salinity	37.8	psu	M	5
Refractory carbon conc	TOC0	1	%	I	4
Maximum rate FeS production	rFeS	0.5	cm^3 $nmol^{-1}$ d^{-1}	I	1/4
Max rate anaerobic oxidation methane	rAOM	800×10^{-6}	cm^3 $nmol^{-1}$ d^{-1}	I	1/4
Surface porosity	por0	0.83	–	I	–/5
Deep porosity	pordeep	0.65	–	M/C	–/5
Porosity decay coefficient	porcoeff	2	cm	M/C	–/5
Rate of sulphide-mediated iron reduction (oxyhydr)oxidesA	rH2Sfeoxa	1.2×10^{-3}	cm^3 $nmol^{-1}$ d^{-1}	M/C	–/5
Rate of reoxidation of H2S by MnOxA	rH2SMnoxa	1.7×10^{-3}	cm^3 $nmol^{-1}$ d^{-1}	C	6
Rate of reoxidation of Fe with MnOx	rMnFe	6.5×10^{-6}	cm^3 $nmol^{-1}$ d^{-1}	C	2

Note. (I) independent parameters derived from experiment or field observation external to actual data being simulated (C) constrained parameters obtained from a range of literature sources (M) model-derived parameters fitted to the observed data (O) imposed from observed field data. FDET stands for fast detritus (labile carbon) and SDET for slow detritus (semirefractory carbon). Literature sources includes (1) Pastor et al. (2011c), (2) Soetaert et al. (1996), (3) Ait Ballagh et al. (2021), (4) Rassmann et al. (2020), (5) Wang and Van Cappellen (1996), and (6) Wijsman et al. (2002).

21699291, 2025, 6, Downloaded from https://agupubs.onlinelibrary.wiley.com/doi/10.1029/2025JC022414 by Universitetsbiblioteket, Wiley Online Library on [07/01/2026]. See the Terms and Conditions (https://onlinelibrary.wiley.com/terms-and-conditions) on Wiley Online Library for rules of use; OA articles are governed by the applicable Creative Commons License

grows, both the enrichment factor and the thickness of the deposit ($Z_{\text{pert}}(t)$) are linked, making the enrichment factor a time-dependent parameter ($\alpha(t)$).

$$C_{\text{org}}^{\text{flood}} \approx \alpha(t)\, C_{\text{org}}^{i}(t)\big|_{0}^{z_{\text{pert}}} = \alpha(t)\frac{\int_{0}^{z_{\text{pert}}} C_{\text{org}}^{i}(t^{-})\,dz}{Z_{\text{pert}}(t)} \begin{cases} \alpha(t) < 1, & \text{if } \text{TOC}_{z_{\text{pert}}} < \text{TOC}_{\text{old}} \\ \alpha(t) > 1, & \text{if } \text{TOC}_{z_{\text{pert}}} > \text{TOC}_{\text{old}} \end{cases} ; \; i = 1(\text{fast}), 2(\text{slow}) \quad (3)$$

where $C_{\text{org}}^{i}(t^{-})$ is TOC just before the deposition event (t^{-}). See Nmor et al. (2022) for further detailed implementation of this instantaneous flood deposition formulation.

The advancement in this event-driven deposition algorithm provides some realism to how natural dynamic sedimentary systems work, albeit with an extra layer of complexity and parameterization constraint to the model. It is important to note that the model assumes net deposition here while ignoring erosion, particle reworking, and redistribution of the material following these pulse events. This simplification is apt here, where sedimentological references to the deposition-erosion cycle indicate that erosion after each large storm event is at most 2–4 cm, while sediment deposition could be more than 10–30 cm during this kind of event (Dufois et al., 2014; Marion et al., 2010).

2.5. Model Simulation

2.5.1. Simulation Strategies

2.5.1.1. Nominal Simulation for Flood Deposition 2008

The numerical procedure for solving the underlying reactive transport equation capturing the processes in Section 2.2 have been previously discussed (Nmor et al., 2022). In summary, the simulation was carried out in the sediment grid layer of 100 cm thickness with intermittent deposition events treated as an abrupt change to the model dynamics at specified time intervals (see Figure 1).

The model simulation was conducted over 2 years starting in January 2008 in order to capture the hydrological regime of 2008. It was started with a steady-state simulation and spin-up for 2 years to achieve dynamic equilibrium, thereafter called the "*initial state*." The main simulation was then run for 2 years (January 2008–December 2009). The model can be configured to include multiple events; therefore, the decision on the number and timing of deposition events to implement in order to adequately describe the observed data was made considering the prevailing hydrodynamical and sedimentological constraints within the sampling time window (Cathalot et al., 2010; Pastor et al., 2018). We used data from the last river gauging station in Arles (40 km upstream the river mouth) to examine river discharge and total suspended matter (TSM). Figure 1 depicts the timing of the deposits. While the TSM data may constrain timing and not necessarily the magnitude of deposition at any particular site, a detailed analysis of the river discharge and the corresponding TSM data suggests a power-law relationship (Pont et al., 2002), and further examination of the temporal variability in both data sets indicates the occurrence of a minor flood event between the two major deposits (spring and fall deposition) (Figure 1). Following this analysis, three sequential flood deposition simulations were performed. The first corresponds to a *major* spring flood event with low organic carbon content and a sediment deposition of 30 cm. The fall flood, which delivered 10 cm of sediment enriched in organic carbon and reactive minerals, was described as the second major event (see Cathalot et al. (2010) for sediment deposition in May and November 2008).

Because the intermediate third event was missed by the sampling campaign in 2008, we chose a simple approach by assuming that the event is relatively mild in comparison to the two major floods, as evidenced by discharge and TSM data, as well as down core sediments retrieved in September and October (around the limited deposition event), which show little evidence of a large deposition (Cathalot et al., 2010). The enrichment factor (α—see section-Section 2.4 for definition) used in the simulations as well as the thickness of the deposited layer is provided in Table 3.

With the simulation strategy discussed above, our goal is to obtain the best possible representation of transient dynamics associated with these short-term events. To that end, it is critical to distinguish between the initial state (i.e., preflood) and the solution from steady state.

21699291, 2025, 6, Downloaded from https://agupubs.onlinelibrary.wiley.com/doi/10.1029/2025JC022414 by Universiteitsbibliotheek, Wiley Online Library on [07/01/2026]. See the Terms and Conditions (https://onlinelibrary.wiley.com/terms-and-conditions) on Wiley Online Library for rules of use; OA articles are governed by the applicable Creative Commons License

21699291, 2025, 6, Downloaded from https://agupubs.onlinelibrary.wiley.com/doi/10.1029/2025JC022414 by Universiteitsbibliotheek, Wiley Online Library on [07/01/2026]. See the Terms and Conditions (https://onlinelibrary.wiley.com/terms-and-conditions) on Wiley Online Library for rules of use; OA articles are governed by the applicable Creative Commons License

Table 3
Event-Specific Parameters Used in the Model

	Event date	Data collection	Thickness (cm)	α					
				C_{org}^{fast}	C_{org}^{slow}	$FeOOH_A$	$FeOOH_B$	MnO_{2A}	MnO_{2B}
Spring	29 May 2008	08 June 2008	30	0.5	0.7	0.3	0.3	1	2
Intermediate	05 September 2008	06 September 2008	3	0.5	0.7	1.0	1.5	1	2
Fall	08 November 2008	08 December 2008	10	20.0	5.0	8.0	2.0	10	5

Note. Deposit thickness (cm) and the enrichment factor (α) as well as timing of event and data collection.

The initial state after the spin-up is stable and represents a long-term stable state. It is compared to the data collected a few days before the spring flood in May, which might still be undergoing some evolution linked to the previous winter/early spring flood deposition. Therefore, the match between the initial state of the model and the data collected before the flood can be suboptimal. Nevertheless, the data set from late May is the closest to the initial state and is used in this paper. Furthermore, to comprehend the evolution of the diagenetic system after flood depositions, this study attempted to find a solution that described the overall features and the general pattern observed in the entire data set including initial and postflood states, with a focus on the spring and fall events. Hence, each model outputs before and after the floods can show some level of discrepancy with the observations, but the general pattern of evolution needs to be adequately represented by the model.

Furthermore, the model analysis performed within this simulation was decomposed into two components corresponding to the spring and fall flood events. This calculation involved integrating any model quantity, variable or metrics of interest over a relaxation timescale. The relaxation interval is defined as the timescale over which a particular variable subject to the perturbation signal caused by flood deposition becomes indistinguishable from background variation (see Nmor et al. (2022) for introduction and Section 2.5.2). Thus, the biogeochemical effects of the different flood deposition events can be compared.

2.5.2. Relaxation Time

The relaxation timescales of the various biogeochemical pathways are calculated in the same way as Nmor et al. (2022). However, a minor change in the methodology is presented using a more analytical rather than numerical approach in order to consider processes or rates, which may have a longer timescale of relaxation beyond the interval of two successive depositions. Thus, assuming that the difference between two consecutive porewater profiles (P) will diminish over time following a perturbation (see an equivalent representation in Equation 22 in Nmor et al. (2022)). This diminishing difference between the profiles, when vertically integrated will follow an exponential trend relaxing toward its preflood state. Such a pattern can be approximated by a first-order differential equation as follows:

$$\frac{dP}{dt} = -\lambda P \tag{4}$$

A secular rate of decay λ can be estimated from the time series of the successive concentration profile captured by P. This is especially true for situations where there is no internal background forcing, such as the configuration investigated in this work. This decay coefficient can be calculated by solving Equation 4 as follows:

$$P = P_0 e^{-\lambda t} \tag{5}$$

where P_0 denotes the initial value of the vertically integrated differences between the flood and preflood profiles. This equation can be regressed to determine the λ that best matches the distribution of P. The characteristic timescale can then be defined as the timescale over which a fixed percentage of the profile is said to be similar to previous profiles (Equation 6). For example, in this paper, a 95% recovery is assumed; thus, for all practical purposes, the profiles for a variable/rate in question is more or less indistinguishable from its preflood state. Similar analogy to e-folding timescale can be made here.

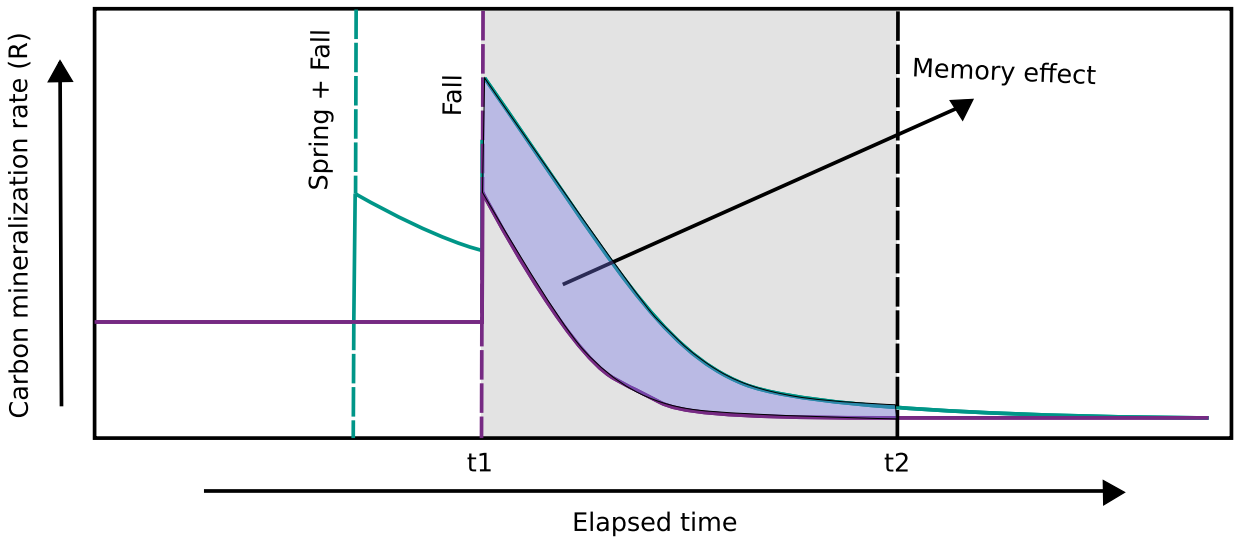

Figure 2. Schematic of the interaction between two floods on biogeochemical processes in the sediment. The memory effect of the spring flood on the subsequent fall period flood is defined as the difference between time-integrated rate of biogeochemical process between t1 and t2 for one flood (fall) and two successive floods (spring + fall).

An advantage of this approach is that we can derive an analytical formulation of this relaxation timescale using Equation 5. For example, a relaxation timescale ($\hat{\tau}_\eta$) for any arbitrary time threshold η can be written as follows:

$$\hat{\tau}_\eta = \frac{1}{\lambda} ln \frac{100}{100 - \eta} \quad (6)$$

where τ_η is the relaxation timescale required to restore the system to η % of its preflood state. This analytical derivation allows us to infer the long-term outcomes of these repeated transient responses to constant environmental perturbation. Another advantage of this method is the possibility to investigate the temporal characteristics of sediment biogeochemistry if a perturbed system never reaches an ultimate asymptotic state (as in the case of an environment that is sufficiently variable). It is important to note that η should not be fixed at a 100% recovery as this will equate to an infinite relaxation timescale. Discretion on the reasonable limit of threshold to which system can be deemed representative of the preflood scenario should be applied here. For the application discussed in this paper, a 95% recovery threshold was used.

2.5.3. Memory Effect for Flood Deposition in 2008

A natural consequence of the chain of instantaneous flood depositions at various times in the simulation is the possibility of the different biogeochemical processes incorporating a memory effect (i.e., the time influence of a former event on the evolution of the current one). Given that relaxation times for some species such as DIC and SO_4^{2-} are up to 5 months (Nmor et al., 2022), they may overlap with other deposition events. The occurrence of multiple flood deposition events and their interactions could be important drivers of biogeochemical processes in coastal sediment and the resulting fluxes.

We investigate to what extent these sequential flood events might influence the biogeochemical pathways of carbon by conducting another slightly different simulation from the nominal reference simulation detailed above by omitting the first deposition (i.e., spring flood). This provides a way to quantify the changes in the reaction pathways with regard to different situations in a given hydrological year: two successive floods (spring and fall) for which their relaxation may overlap or one flood only (fall). The comparison of the two situations can provide a quantification of the feedback dynamics of floods and their succession on sediment biogeochemistry (Figure 2).

Given the occurrence of two flood events in one hydrological year, we proceeded to diagnose the effect of succession of floods on the biogeochemical rates. To this end, we estimated the memory effect of the flood by simulating two flood events: The first simulation is the same as the simulation performed above where the two

21699291, 2025, 6, Downloaded from https://agupubs.onlinelibrary.wiley.com/doi/10.1029/2025JC022414 by Universiteitsbibliotheek, Wiley Online Library on [07/01/2026]. See the Terms and Conditions (https://onlinelibrary.wiley.com/terms-and-conditions) on Wiley Online Library for rules of use; OA articles are governed by the applicable Creative Commons License

depositions occurred within the simulation window, that is, initialized with spin-up profiles and two sequential flood events. The second simulation is performed without the first spring flood (i.e., only second flood effect initialized from the spin-up profiles) (Figure 2). The relative difference in the integrated rates of biogeochemical processes averaged from the start of the fall flood deposition (t1) to the end of the relaxation (t2) in both scenarios indicates the magnitude of the memory effect (ME):

$$\mathrm{ME}(\%) = \frac{\int_{t1}^{t2} R^{\mathrm{spring+fall}} dt - \int_{t1}^{t2} R^{\mathrm{fall}} dt}{\int_{t1}^{t2} R^{\mathrm{fall}} dt} \times 100 \quad (7)$$

where $t1$ and $t2$ are the time intervals in which the memory effect of the spring flood on the fall flood is estimated. Each term of the numerator in Equation 7 is basically the time-integrated difference of any vertical integrated rate biogeochemical process R^i within a time window between $t1$ and $t2$. $t1$ is the fall flood deposition and $t2$ is 6 months later, encompassing the relaxation time of the system. In essence, this numerical experiment implicitly assumed no other deposition occurs in between the period when this calculation is performed.

3. Results

3.1. Model-Data Evaluation

3.1.1. Global Performance of Model Prediction

The model was validated with the complete data presented in the two flood events in 2008 as described in Pastor et al. (2018) for station A. Here, we only show results for key porewater species that capture the sediment response following these events. The skillfulness of the model in describing the observed vertical distributions and their temporal variations was diagnosed using a Taylor diagram (Taylor, 2001), which summarizes the goodness of model fit relative to the data. We considered the depth dependence variability, model-data bias, and model-data correlation as three different measures of the model's performance. The variability is represented by the standard deviation of the observed and modeled values (x and y axes of the graphs) with its magnitude measured as the radial distance from the origin of the plot (dashed line in Figure 3). A value of 1 indicates a fair representation of vertical variability in the data while value above and below 1 signifies an over or underestimation of the true variability in the data. The bias measures the model-data difference (root mean square, RMS) as well as the model standard deviation, which are normalized by dividing the RMS and standard deviation by the observation's standard deviation. The centered root mean square error (RMSE) is the concentric dashed lines originating from the "observed" point. The further the model is from the observed point, the bigger its bias is. As such, a value close to 0 reflects a good fit of the model to the observation. The "observed" point is plotted on the x-axis at a unit length distance from the origin in this case. As such, we can succinctly visualize, by how much the model fits to the data. This nondimensional deviation also has the advantage of allowing model-data statistics for different flood types/events to be compared on the same plot. The model-data correlation is captured by the correlation coefficient and is shown on the arc line with points, which lie closest to the x-axis, having the highest correlation.

Here, the simulation of oxygen during the spring flood shows lesser bias to the oxygen data than the fall despite the fact that both events display reasonably high and similar correlations. The model prediction for SO_4^{2-} performed better in both deposition periods with a correlation of 0.96 and 0.94 for spring and fall floods, respectively, and a slightly better overall metrics in the former than the latter (Figure 3). DIC simulated by the model during the spring deposition showed better correspondence with the measured data (high correlation = 0.98) in terms of correlation with the data and a reasonable representation of the variability in the porewater DIC (±0.8 from true variation i.e., more than half the true variability observed in the data) in comparison to the fall model prediction. Among the reduced metal species, the predicted profile for dissolved Mn was significantly more faithful to the data across both events (with a higher correlation coefficient and lower RMSE) than the predicted profile for dissolved Fe. The vertical variability observed in the fall porewater data is better captured in both cases. Ammonium showed decent model fit with the data in both events with strong correlation observed across both seasons ($r > 0.7$) (Figure 3).

21699291, 2025, 6, Downloaded from https://agupubs.onlinelibrary.wiley.com/doi/10.1029/2025JC022414 by Universiteitsbibliotheek, Wiley Online Library on [07/01/2026]. See the Terms and Conditions (https://onlinelibrary.wiley.com/terms-and-conditions) on Wiley Online Library for rules of use; OA articles are governed by the applicable Creative Commons License

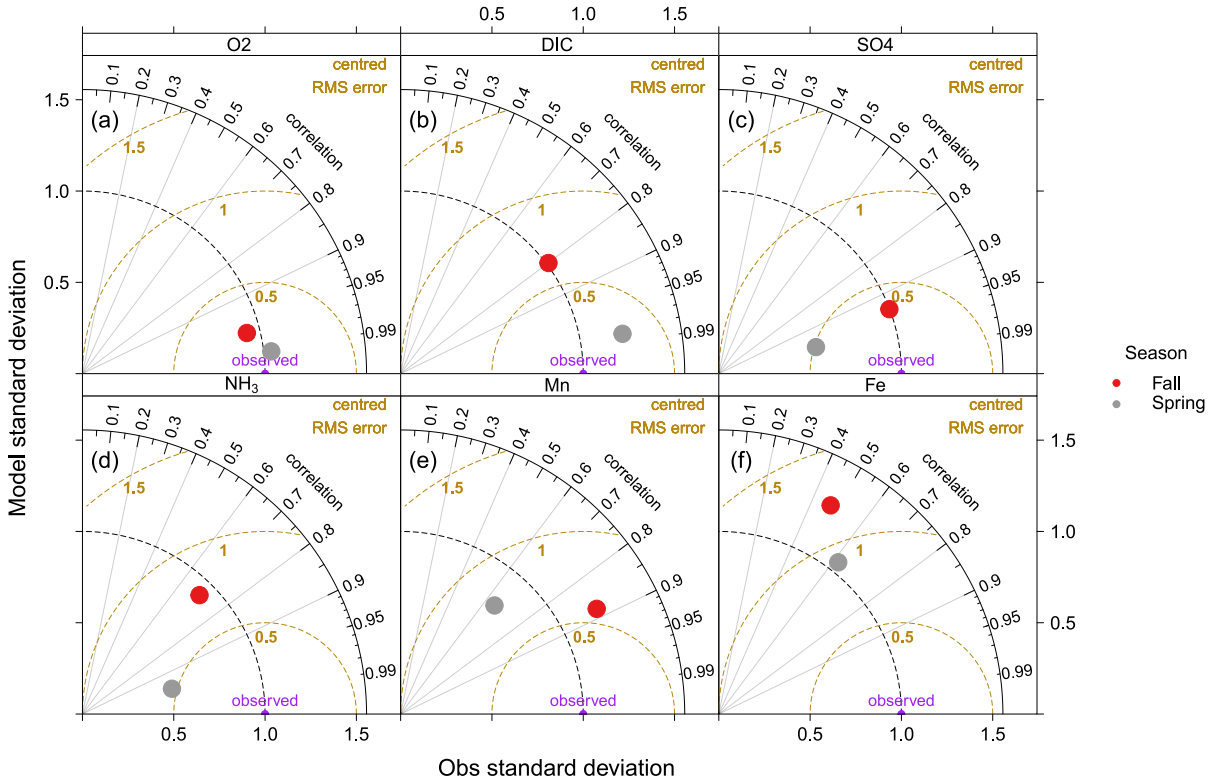

Figure 3. Taylor diagram of goodness of fit between model simulation and data for (a) oxygen, O_2, (b) dissolved inorganic carbon, DIC, (c) sulfate, SO_4^{2-}, (d) ammonium, NH_4^+, (e) manganese, Mn^{2+}, and (f) iron, Fe^{2+}. Gray and red dots denote the spring and fall deposition simulation with the normalized observed standard deviation shown in purple. See text for explanation and interpretation.

3.2. Evolution of Porewater Profiles

3.2.1. Preflood Situation

The porewater profiles prior to the occurrence of the massive flood input in May–June, referred to as the "initial state," reflected a system at the end of relaxation after a winter perturbation or the "quasi-steady-state" condition (Figure 4). Given this before spring deposition, the model preflood situation managed to capture the essence of the main biogeochemical features inherent in the prodelta sediment. A simulated TOC profile follows the basic trend in TOC with higher OC content (2%) below 5 cm and high concentration around 20 cm. This vertical variability is typical of sediment accumulation under flood regimes. The initiation of OC oxidation led to a shallow oxygen penetration depth (1.5 mm) before the flood and complete sulfate exhaustion around 20 cm. It is noteworthy that no dissolved sulfide is simulated which reflects the observed absence of sulfide in porewaters. DIC and NH_4^+ increased with depth to an asymptotic concentration of 60 mM and 3 mM respectively, a feature captured by the model. Furthermore, dissolved Mn was observed with enhanced concentration between 5 and 10 cm with maximum concentration of 100 μM, which was captured by the model (Figure 4). The model dissolved Fe profile, similarly, demonstrated agreement with the measured porewater Fe in the upper 10 cm, with a subsurface maximum of 560 μM fed by iron reduction linked to the mineralization of organic carbon-enriched sediment. However, below this subsurface peak, predicted dissolved Mn and Fe deviated systematically from the data with lower simulated dissolved Mn and larger dissolved Fe than measured at depth.

3.2.2. Generalized Flood Deposition (Spring 2008)

The delivery of terrestrially derived sediment particles peaked within 10 days after the flood began, with a massive accumulation of sediment as high as 30 cm observed at the study site (Cathalot et al., 2010).

The simulated profiles 10 days after the flood event were able to capture the dominant spatial variation in the porewater species. Given the refractory nature of the deposited sediment, oxygen was present in the surface

21699291, 2025, 6, Downloaded from https://agupubs.onlinelibrary.wiley.com/doi/10.1029/2025JC022414 by Universiteitsbibliotheek, Wiley Online Library on [07/01/2026]. See the Terms and Conditions (https://onlinelibrary.wiley.com/terms-and-conditions) on Wiley Online Library for rules of use; OA articles are governed by the applicable Creative Commons License

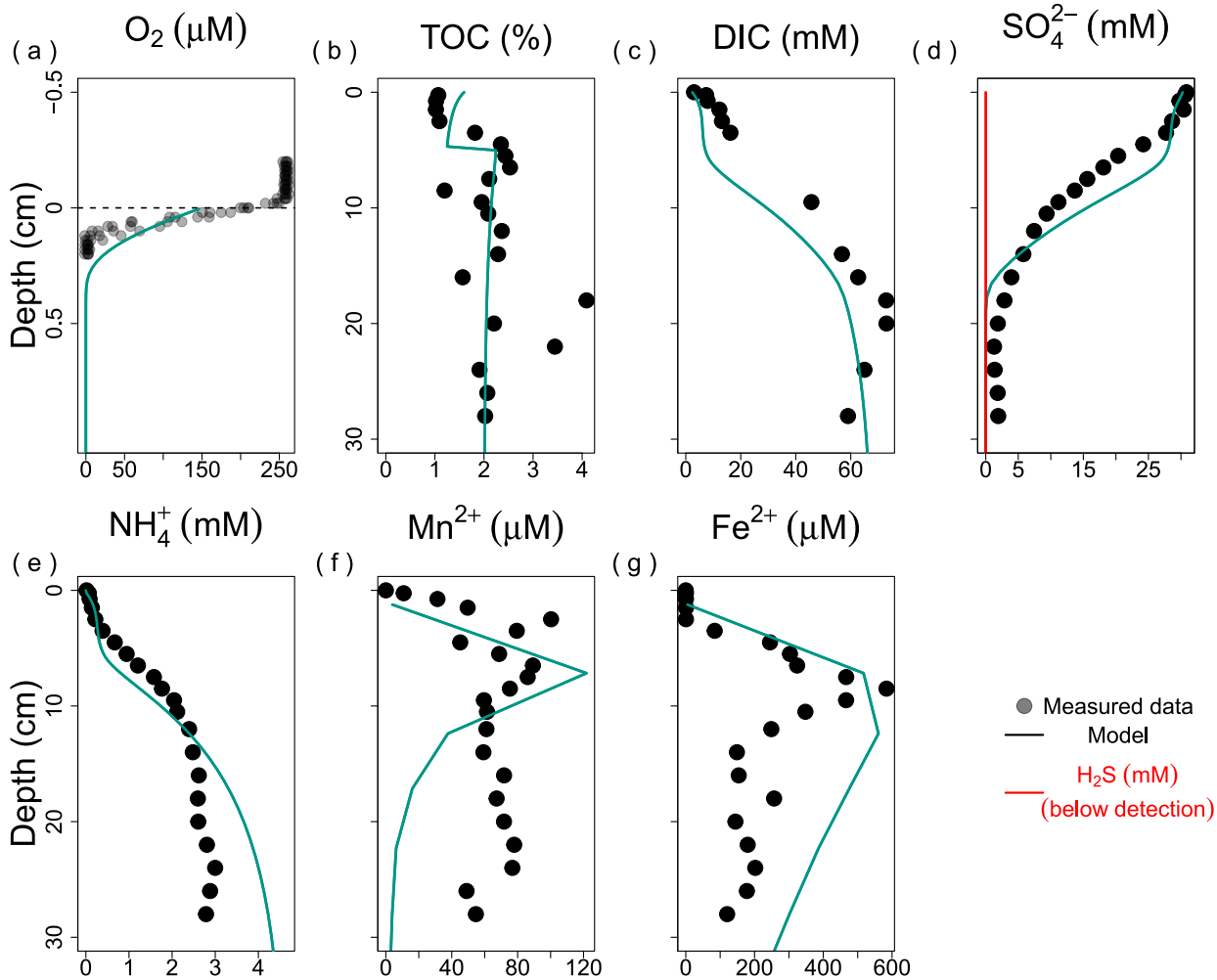

Figure 4. Model-data fit against observed data for (a) oxygen, O_2, (b) total organic carbon, TOC, (c) dissolved inorganic carbon, DIC, (d) sulfate, SO_4^{2-} and hydrogen sulfide, H_2S, (e) ammonium, NH_4^+, (f) manganese, Mn^{2+}, and (g) iron, Fe^{2+}. Data collected on the 29th of May 2008 at Station A before spring flood (Pastor et al., 2011c). Note, the vertical scale of O_2 extend to the overlying bottom water.

sediment down to 6.8 ± 0.04 mm (Figure 5). The model estimate of the oxygen penetration depth is 6.3 mm. The spatial variation of ammonium was well captured by the model with the low but constant (NH_4^+) at the surface down to the depth of the newly deposited layer (30 cm).

Sulfate concentration during this spring event was constant in the upper 30 cm of the sediment, equaling the value of the bottom water concentration trapped in by the flood layer (Figure 5). Underneath the layer, the sulfate concentration in the model as well as the data decline with depth and were characterized by strong sulfate reduction (80 mmol C $m^{-2}d^{-1}$) within this zone. The by-product of this mineralization, dissolved inorganic carbon (DIC), showed a mirrored pattern: with a low but almost constant concentration from the surface down to the depth of 30 cm and a large increase below. Total DIC production beyond this depth was 90 mmol C $m^{-2}d^{-1}$ and was majorly driven by the relatively rich buried OM below the former interface. The model-calculated correlation between porewater SO_4^{2-} and DIC indicates that the additional flood deposition induced an enhanced DIC production due to the complete exhaustion of SO_4^{2-} and a growing importance of methanogenesis (10 mmol $m^{-2}d^{-1}$), especially just slightly below the zone of sulfate depletion (45 cm) (Figure 5). Fe^{2+} and Mn^{2+} are described in a separate section (Section 3.2.4).

21699291, 2025, 6, Downloaded from https://agupubs.onlinelibrary.wiley.com/doi/10.1029/2025JC022414 by Universitetsbiblioteket, Wiley Online Library on [07/01/2026]. See the Terms and Conditions (https://onlinelibrary.wiley.com/terms-and-conditions) on Wiley Online Library for rules of use; OA articles are governed by the applicable Creative Commons License

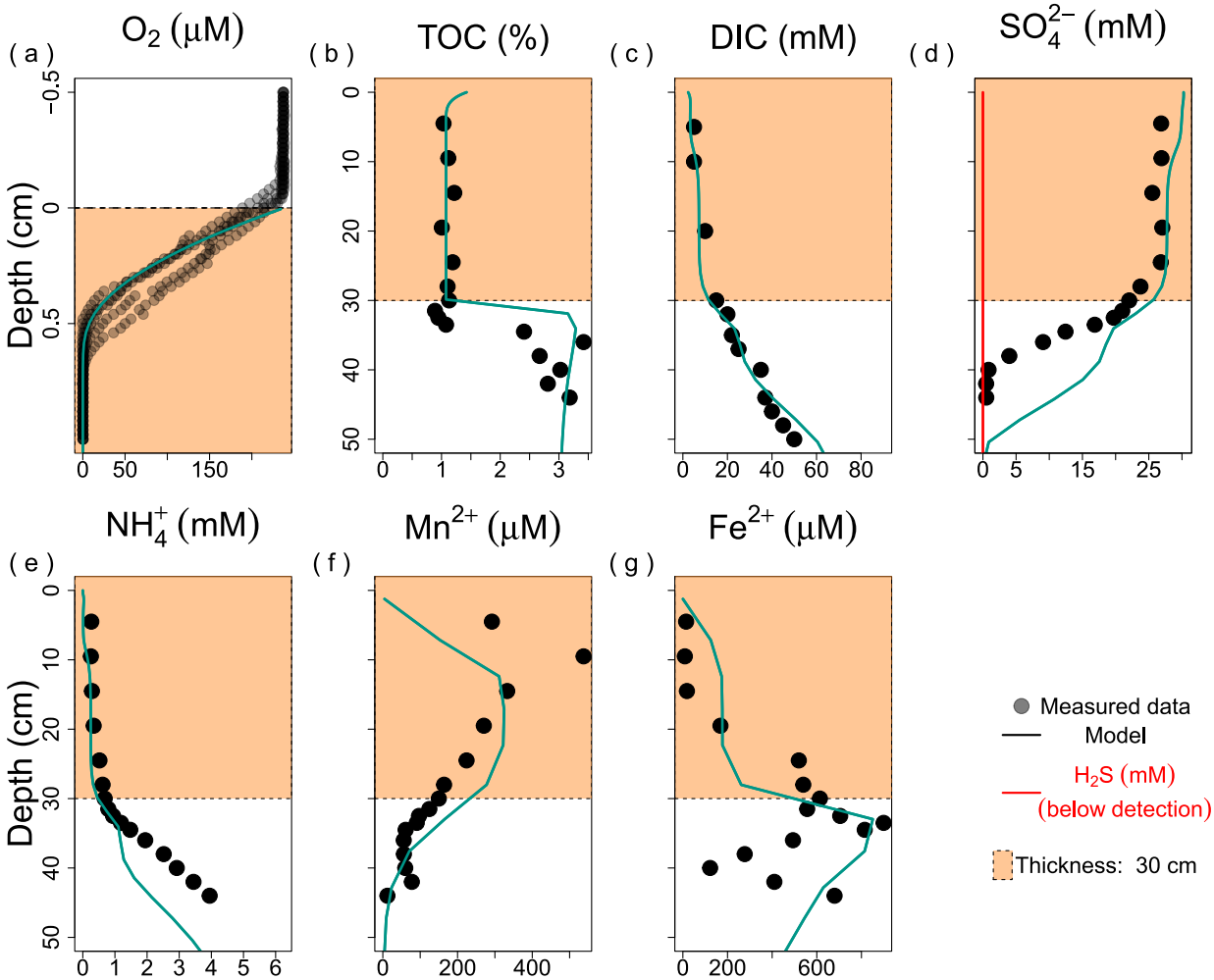

Figure 5. Model-data fit against observed data for (a) oxygen, O_2, (b) total organic carbon, TOC, (c) dissolved inorganic carbon, DIC, (d) sulfate, SO_4^{2-} and hydrogen sulfide, H_2S, (e) ammonium, NH_4^+, (f) manganese, Mn^{2+}, and (g) iron, Fe^{2+} during the May/June flood. Data were collected on the 6th of June 2008 at Station A. The orange section represents the new flood deposit. Note that the vertical scale of O_2 extends to the overlying bottom water.

3.2.3. Cenevol Flood Deposition (Fall 2008)

The contrasting flood deposition observed in the fall of 2008 and the subsequent evolution of the sediment and porewaters were well reproduced by the model. One month after the flood, oxygen penetrated down to a depth of 2.2 mm with stronger oxygen demand due to the labile nature of the deposited OM. This is larger, but close to the range of the observed in situ/ex situ oxygen penetration 1.6 ± 0.3 mm. DIC increased with depth including the flood layer, with the model matching the spatial variation of the measured porewater DIC. The sulfate concentration decreased from 30 mM at the SWI to about 15 mM at a depth of 10 cm (Figure 6) and remained constant. During this period, sulfate reduction accounted for 94% of a flood-induced mineralization rate of 370 mmol m^{-2} d^{-1} (Figure 6).

3.2.4. Fe-Mn Cycling Under the Episodic Flood Event

The difference between the flood deposits of the spring and fall floods is also revealed in the distribution and concentration of dissolved iron and manganese. A striking feature in the spring flood is the rapid and large accumulation of dissolved Mn in the newly deposited layer (well reproduced by the model) and the lack of dissolved iron in this same layer, also captured by the model. On the contrary, after the fall flood, the situation, a month after deposition, shows a large accumulation of both dissolved Fe and Mn in the porewater, also well captured by the model.

21699291, 2025, 6, Downloaded from https://agupubs.onlinelibrary.wiley.com/doi/10.1029/2025JC022414 by Universitetsbiblioteket, Wiley Online Library on [07/01/2026]. See the Terms and Conditions (https://onlinelibrary.wiley.com/terms-and-conditions) on Wiley Online Library for rules of use; OA articles are governed by the applicable Creative Commons License

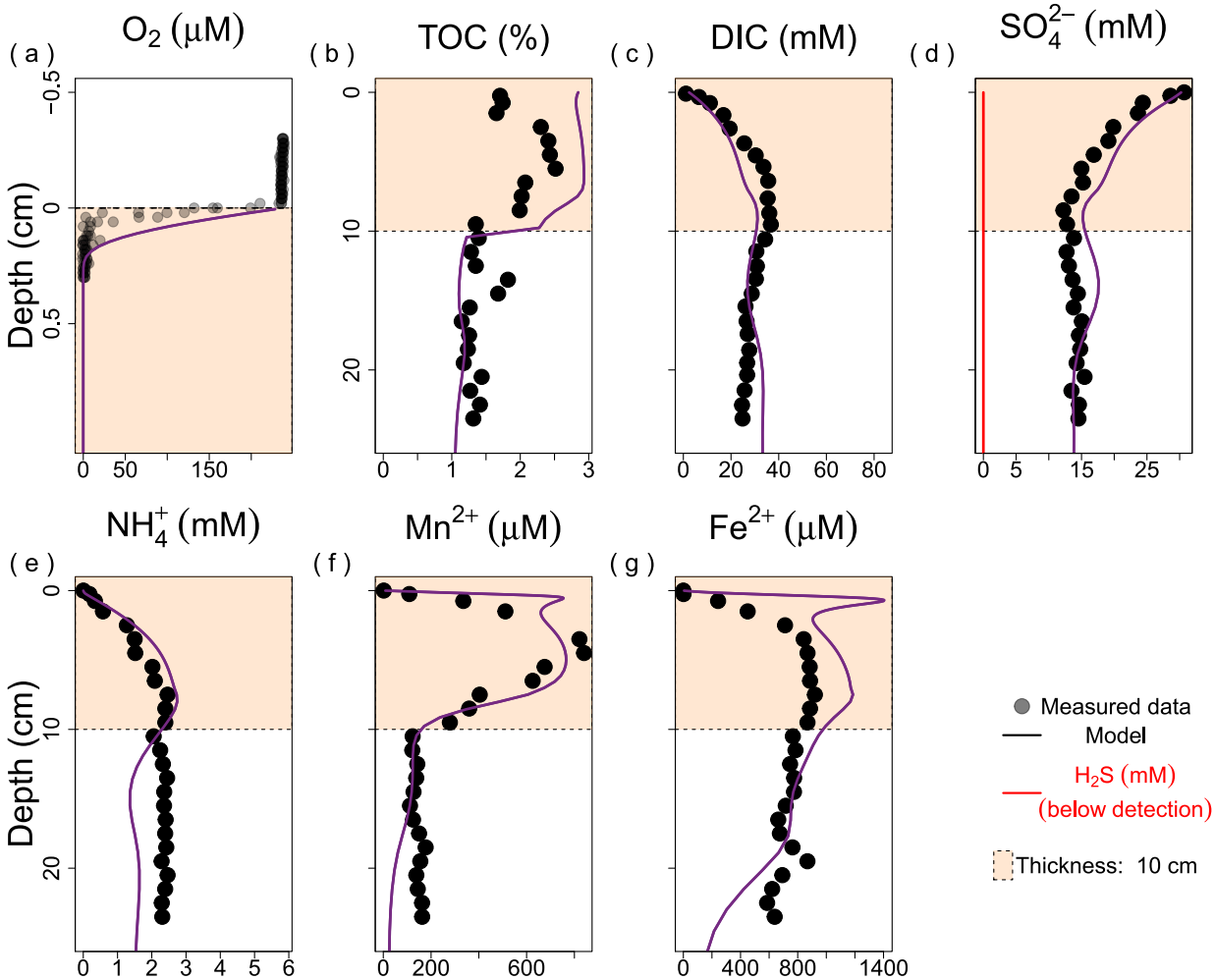

Figure 6. Model-data fit against observed data for (a) oxygen, O_2, (b) total organic carbon, TOC, (c) dissolved inorganic carbon, DIC, (d) sulfate, SO_4^{2-} and hydrogen sulfide, H_2S, (e) ammonium, NH_4^+, (f) manganese, Mn^{2+}, and (g) iron, Fe^{2+} during the November flood collected on the 8th of December 2008 (26 days after the flood event—11th of November 2008) at station A. Note that the vertical scale of O_2 extends to the overlying bottom water.

In general, when compared to the measured porewater profiles during the two floods, the model simulation reproduced the vertical structure of the data and suggest a transient, nonsteady state condition of the dissolved Fe and Mn. In order to simulate these different flood deposits, a background flux of 50 and 10 mmol m^{-2} d^{-1} for iron and manganese oxides, respectively, was imposed in the model upper boundary. The availability of this particulate Fe and Mn as well as organic carbon at the initial state resulted to a release of dissolved metals in the porewater. Our model simulation indicates that at the time of sampling in June 2008, the dissolved Mn peak had already migrated from a depth of 30 cm (below the newly deposited layer) and was enriched by a factor of 4 to around 10 cm where the observed Mn maximum was detected (Figure 5). At this particular depth of 10 cm, the model matches the trend but not exactly the amplitude of the observed variation (data—540 vs. model— 320 µM). Below this reactive front, Mn decreases with depth in both the observed and simulated porewater. Both the measured data and model prediction suggest a complete reduction of reactive MnO_2 and negligible release of dissolved Mn at depth.

In contrast, dissolved Fe during the spring flood period was lower in the new flood layer in the measured data and increased with depth to a concentration of 850 µM at the former SWI (now buried underneath the deposited layer) (Figure 5). In this zone, nonsteady dynamics was simulated by the model as can be seen in Figure 5, driven by a combination of diagenetic processes involving microbial iron oxide reduction, sulfide reoxidation by Fe oxides,

21699291, 2025, 6, Downloaded from https://agupubs.onlinelibrary.wiley.com/doi/10.1029/2025JC022414 by Universiteitsbibliotheek, Wiley Online Library on [07/01/2026]. See the Terms and Conditions (https://onlinelibrary.wiley.com/terms-and-conditions) on Wiley Online Library for rules of use; OA articles are governed by the applicable Creative Commons License

Table 4
Depth-Integrated Biogeochemical Processes Associated to Iron and Manganese in Spring and Fall Calculated From Time of the Event Deposition Up to a Relaxation Timescale Window of 4 Months

Processes	Spring	Fall
Fe		
Organoclastic FeOOH reduction	25	65
FeOOH reduction by H_2S	53	153
Total FeOOH reduction	78	218
Fe^{2+} oxidation by O_2	4	6
FeS production	29	73
Fe^{2+} oxidation via MnO_2	0.2	0.1
Mn		
Organoclastic MnO_2 reduction	8	7
MnO_2 reduction by H_2S	8	23
MnO_2 reduction by Fe^{2+}	0.2	0.1
Total MnO_2 reduction	16	30
Mn^{2+} oxidation by O_2	0.3	0.2
$MnCO_3$ precipitation	10	24

Note. Relaxation timescale calculated using Equation 6. Rates are in units of mmol m^{-2} d^{-1}.

and FeS precipitation Equation 2. This geochemical horizon in the subsurface layer where dissolved Fe is maximum migrates slowly and persists for a longer period after the spring flood deposition.

In the fall flood, a different vertical profile of the reduced metals emerged. Like the measured data, the model again predicted a large accumulation of dissolved Mn in the flood layer. The subsurface Mn peak of 766 μM within the vicinity of 5 cm shows a good correspondence with the data (840 μM). In contrast to the spring flood where dissolved iron was confined below the new flood layer, Fe^{2+} also accumulated in the fall with a gradual increase from the surface up to 920 μM (vs. 1,100 μM in the model) at 5 cm. The gradient in measured and simulated Fe^{2+} data stabilized to this asymptotic concentration albeit with a slight departure from the model at depth (Figure 6).

The source of these metals in porewater is linked to the reduction of iron and manganese oxides, which differs from the other oxidants utilized because the reductive pathways can occur via biotic and abiotic pathways. By integrating the various reaction pathways affecting dissolved Mn and Fe released over a 4-month window linked to their respective relaxation timescale, our result shows that the sediment is sufficiently reducing to allow the release of the dissolved metals at a faster rate than their removal rate (Table 4). The model calculation suggests that around three-fourth of the depth-integrated reduction of FeOOH during the spring deposition is due to the abiotic reduction by H_2S (53 mmol Fe $m^{-2}d^{-1}$) with a large release of dissolved iron to the porewater during the fall flood event (218 vs. 78 mmol Fe $m^{-2}d^{-1}$). Meanwhile, the depth-integrated rate of microbial iron reduction during the spring flood event (25 mmol Fe $m^{-2}d^{-1}$) represented a limited amount of FeOOH reduction.

This redox cycling in the sediment can be quantified using the recycling efficiency number, E^i (Equation 8) (Rabouille & Gaillard, 1991; Wang & Van Cappellen, 1996), adapted for a time-dependent model as follows:

$$E^i = \frac{R^i_{\text{red}}}{J + R^i_{\text{red}}} \tag{8}$$

where R^i_{red} is the depth-integrated rate of Fe or Mn reduction at each time point, i and J are the deposition fluxes of reactive metal oxides. Values near 1 indicate a very strong internal cycle, whereas values below 0.2 indicate that metal oxide reduction is driven by the input flux. Using this calculation, the model suggested that the sediment reactivity is under intense recycling in both flood events (>0.5) especially right after the flood deposition. In this case, the efficiency number jumps from 0.58 to 0.65 for Fe and from 0.26 to 0.71 for Mn in the spring. The recycling potential was slightly higher during the fall flood event for both Mn and Fe (0.71 and 0.97, respectively) than the spring flood (Figure 7).

3.3. Mineralization Pathways and Biogeochemical Fluxes

Following calibration of the model with the data, we extracted time series fluxes of dissolved species across the SWI, as well as calculated vertically integrated rates.

3.3.1. Exchange Across the Sediment-Water Interface

The model indicates that a reduced oxygen consumption follows the introduction of the 30-cm deposit of the spring flood sediment as observed by the total oxygen flux or total oxygen uptake (TOU) across the SWI. Model sediment O_2 flux declined from 14.67 to 6.59 mmol O_2 $m^{-2}d^{-1}$ immediately after the first major deposition rebounding back within 15 days to its preflood level. It is worth noting that this range of O_2 flux encompasses the measured flux snapshot (see: Section 3.2.2 and Figure 8). Modeled total oxygen flux across the sediment-water interface (SWI) during this period was 9 mmol O_2 $m^{-2}d^{-1}$ while the measured diffusive flux was

21699291, 2025, 6, Downloaded from https://agupubs.onlinelibrary.wiley.com/doi/10.1029/2025JC022414 by Universiteitsbibliotheek, Wiley Online Library on [07/01/2026]. See the Terms and Conditions (https://onlinelibrary.wiley.com/terms-and-conditions) on Wiley Online Library for rules of use; OA articles are governed by the applicable Creative Commons License

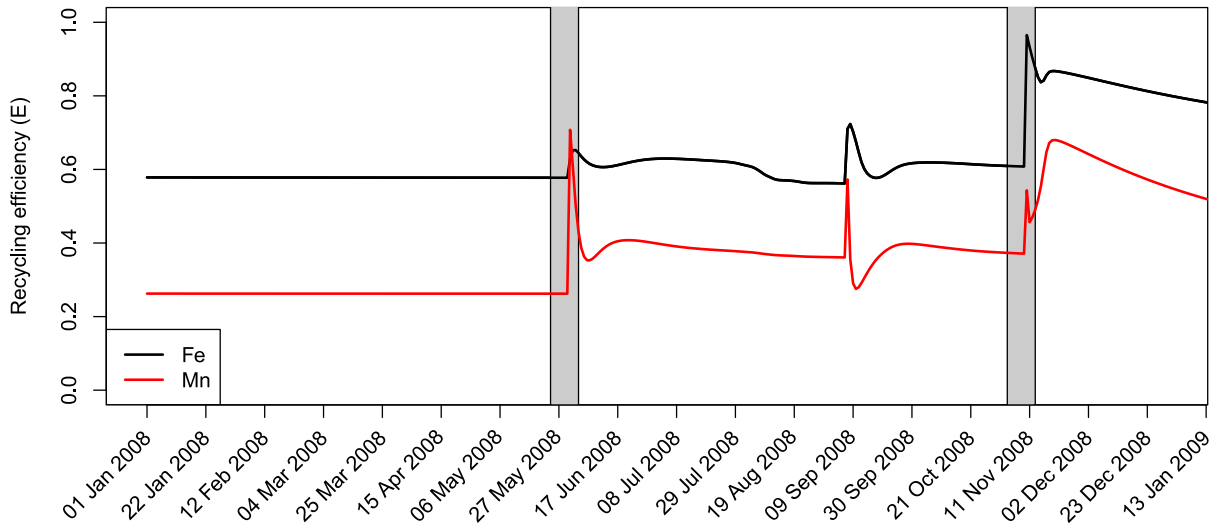

Figure 7. Temporal evolution of recycling efficiency of the metals (iron and manganese) in the sediment. Increasing efficiency numbers imply that the sediment has a high recycling capacity, with a limiting value of 1 indicating that ions cycle only between oxidized and reduced forms inside the sediment without external inputs. The gray bar indicates the time of the flood deposition.

9.2 ± 3.1 mmol O_2 $m^{-2}d^{-1}$. The fall perturbation induced a 65% increase in TOU, which relaxes in 40 days. During this period, modeled O_2 flux (20 mmol O_2 $m^{-2}d^{-1}$) compares well with the observed DOU (16.6 ± 2.9 mmol O_2 $m^{-2}d^{-1}$). In general, oxygen consumption was dominated by oxic mineralization accounting for 56% and 37% of the total oxygen consumption during the spring and fall flood events, respectively.

Throughout the simulation period, the sediment was a source of DIC for the bottom water. The DIC exchange showed a strong contrast between the two floods: during the spring depositional event, the DIC flux dropped to a very low value (86 to 5 mmol C $m^{-2}d^{-1}$) limited by the large influx of semireactive and refractory carbon, whereas in the fall, a large efflux of DIC was estimated (up to 380 mmol C $m^{-2}d^{-1}$) driven by intense surficial production of DIC by microbial activity (Figure 8).

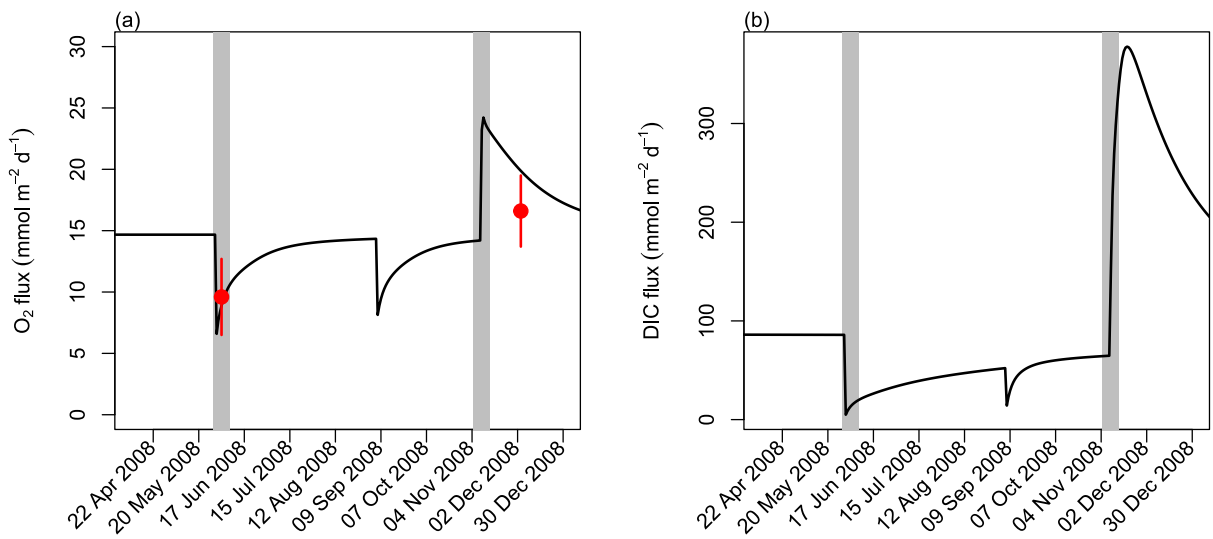

Figure 8. Temporal magnitude of flux (in absolute value) across the sediment-water interface for (a) oxygen and (b) DIC. The red dot in O_2 flux signifies measurement made during this sampling point. The vertical error bar represents the uncertainty in the measured flux. DIC flux is directed out of the sediment while oxygen flux is directed into the sediment. The gray bars indicate the times of the major flood depositions.

21699291, 2025, 6, Downloaded from https://agupubs.onlinelibrary.wiley.com/doi/10.1029/2025JC022414 by Universitetsbiblioteket, Wiley Online Library on [07/01/2026]. See the Terms and Conditions (https://onlinelibrary.wiley.com/terms-and-conditions) on Wiley Online Library for rules of use; OA articles are governed by the applicable Creative Commons License

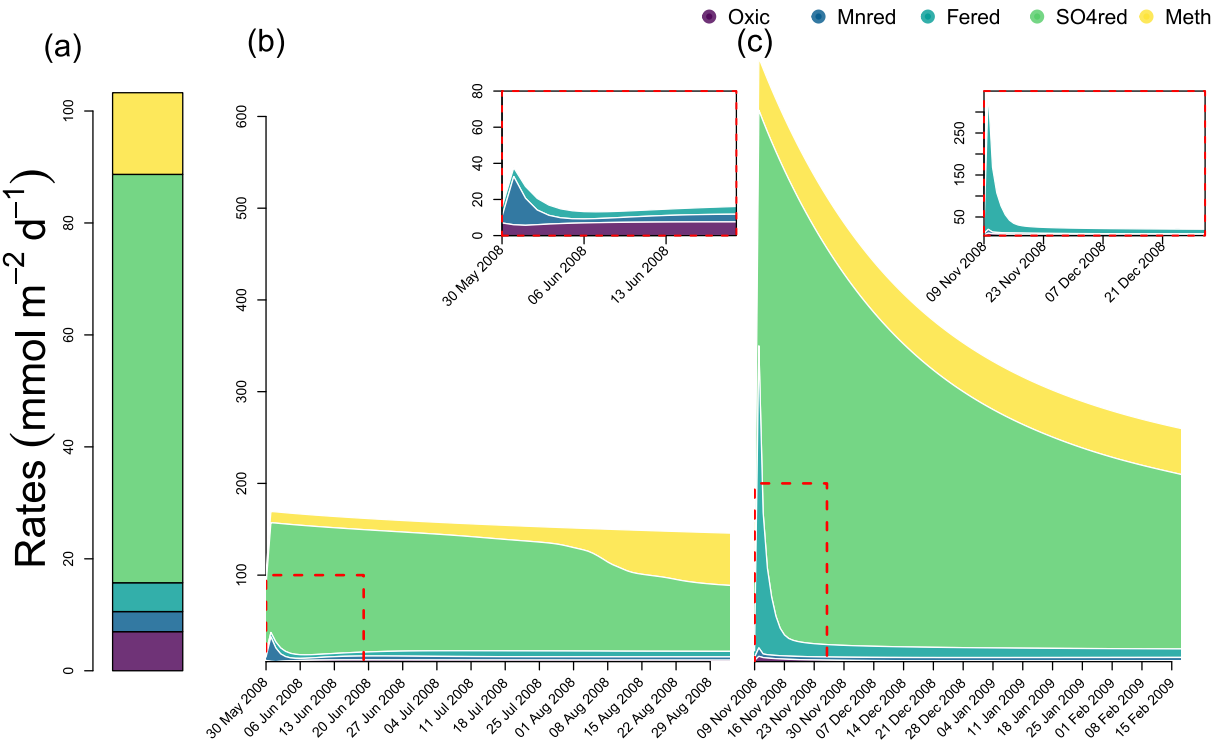

Figure 9. Dynamic evolution of the integrated OC mineralization rate. (a) Initial state of the total organic carbon mineralization rate and different portions of the mineralization pathways. Oxic = aerobic mineralization, Mnred = Mn oxides reduction, Fered = Fe oxides reduction, SO4red = sulfate reduction, and Meth = methanogenesis. (b and c) Dynamic evolution of the total organic carbon mineralization rate and relative importance of the carbon biogeochemical pathways following the successive flood in spring (b) and fall (c) periods. The beginning date is the day of major flood deposits for each event. The insert focuses on pathways with a lower carbon mineralization rate.

3.3.2. Temporal Evolution of Biogeochemical Pathways

The dynamics of the OC mineralization and the partitioning of the different biogeochemical pathways are shown in Figure 9. Before the event, the preflood sulfate reduction (70%) was the dominant mechanism of carbon oxidation, with notable contribution from methanogenesis (14%) and a minor contribution from aerobic respiration (7%). The contribution from metal reduction was equally low (4%). During the first 10 days after the spring flood deposition, oxic mineralization dropped by 25% with only a marginal change in metal reduction. After this initial drop, aerobic respiration increased up to preflood level and stabilized. Similar asymptoticity in metal reduction at a short interval after the deposition was also predicted by the model.

The most remarkable change occurring during this flood is observed in the change in anoxic contribution to the carbon mineralization rate (sulfate reduction and methanogenesis). The model simulated 53% increase (112 mmol m^{-2} d^{-1} vs. 73 mmol m^{-2} d^{-1}) in sulfate reduction from its preflood rate due to the perturbation while methanogenesis is 13% as a result of the deposition (Figure 9). About 20 days after this spring perturbation, both pathways for total carbon mineralization begin to decline as the signature of the deposition begins to wane. By August, the sulfate reduction rate is lower, which reflects the fact that the newly deposited layer in May is poor in labile carbon. The methanogenesis rate still doubles over the same period as it is located below the flood layer where the reactive carbon is located. At this stage, AOM probably peaks and contributes to the consumption of the sulfate below the former interface.

In fall, the large delivery of labile OM produces the greatest change in the sulfate reduction rate (increased from 84 to more than 260 mmol m^{-2} d^{-1}) and although the rate of methanogenesis almost doubled, the contribution of methanogenesis to total mineralization declined by twofold from its preflood level (Panel b 36%–9% Panel c). During this fall flood, only minor changes in aerobic mineralization were simulated except in the first few days. Metal reduction increased tremendously over the first few days after the flood by a factor of 25.

21699291, 2025, 6, Downloaded from https://agupubs.onlinelibrary.wiley.com/doi/10.1029/2025JC022414 by Universiteitsbibliotheek, Wiley Online Library on [07/01/2026]. See the Terms and Conditions (https://onlinelibrary.wiley.com/terms-and-conditions) on Wiley Online Library for rules of use; OA articles are governed by the applicable Creative Commons License

Figure 10. Differential "memory effect" of flood deposition on biogeochemical pathways of carbon. This is calculated as the relative difference between a reference simulation with both spring and fall flood (green dots) versus another simulation with only the fall flood deposition (purple dots). Relaxation timescale is calculated according to Section 2.5.2, and refer to the combined spring + fall perturbation.

3.4. Numerical Experiment: Memory Effect of Flood Deposition on Biogeochemical Processes

Lastly, we examine the effect of cumulative floods (spring and fall) compared to a single fall flood. The memory effect is the relative difference of the cumulative fluxes for the two scenarios (see Section 2.5.2). Results from this analysis show that within the time window after the event, the residual effect of the first flood on biogeochemical pathways was substantial for the anoxic pathways (i.e., sulfate reduction and methanogenesis) but limited for the other pathways. The succession of two floods lead to limited increase/decrease of mineralization rates for all oxidants between the spring + fall floods scenarios compared to second flood (fall event) alone except for iron oxide reduction. Our results indicate that methanogenesis has the largest of the residual effect of the flood with memory-induced influence of 38%. The memory effect seems to be positively correlated with the relaxation timescale calculated for these diagenetic pathways. Indeed, the relaxation period ranges from less than 2 weeks for oxic mineralization, which has <1% memory effect, to 37 months for methanogenesis, which shows a 38% memory effect (Figure 10).

Interestingly, we observed a negative memory effect (−10%) for sulfate reduction following the spring and fall depositions. This follows from the elevated carbon mineralization from this fall deposition enriched with OM rich sediment. In this fall only scenario, sulfate reduction accounts for 77% of total OC mineralization. This is higher than is simulated during the spring and fall combined, where the contribution drops to 68%.

21699291, 2025, 6, Downloaded from https://agupubs.onlinelibrary.wiley.com/doi/10.1029/2025JC022414 by Universiteitsbibliotheek, Wiley Online Library on [07/01/2026]. See the Terms and Conditions (https://onlinelibrary.wiley.com/terms-and-conditions) on Wiley Online Library for rules of use; OA articles are governed by the applicable Creative Commons License

21699291, 2025, 6, Downloaded from https://agupubs.onlinelibrary.wiley.com/doi/10.1029/2025JC022414 by Universitetsbiblioteket, Wiley Online Library on [07/01/2026]. See the Terms and Conditions (https://onlinelibrary.wiley.com/terms-and-conditions) on Wiley Online Library for rules of use; OA articles are governed by the applicable Creative Commons License

4. Discussion

In RiOMar systems, prodeltas and depocenters are zones of rapid accumulation of sediment along the continent-ocean interface, which are typically of terrestrial origin (Blair & Aller, 2012). The quantity and quality of sediment deposited in these depocenters are determined by a variety of parameters, including the precipitation pattern in the watershed and river discharge, the river network and size, and the sedimentological composition of the watershed from which it originates (Aller, 1980; Chakrapani, 2005). As a result, the materials deposited in the river-ocean margins reflect the source and the transport process and hence differ in the properties of organic matter supplied in the majority of depocenters (Bao et al., 2019; LaRowe et al., 2020).

The amount and reactivity of organic matter deposited near the river mouth in the Rhône prodelta varies with the flood type. The material deposited in 2008, for example, distinguishes the spring flood from the fall flood (Cathalot et al., 2010). In comparison to the fall flood, which was characterized by large concentrations of labile OM with relatively recent $\Delta^{14}C$ ($-90‰$ Cathalot et al. (2013)), the spring consists primarily of refractory debris with depleted $\Delta^{14}C$ ($-500‰$), and low OM concentration. These disparities in OM properties can lead to distinct sediment responses, as evidenced by discrepancies in porewater profiles. The difference is reflected in the model by the carbon enrichment factor (α) imposed in both events, with a greater value in the fall than the spring (Table 3), indicating that the organic matter delivered during these events can have significantly different features. However, this relationship is not known and certainly complex as other factors like deposit thickness might influence sediment biogeochemical dynamics in response to flood deposition (Nmor et al., 2022). Here, we discuss the implication of these flood depositions and their types on the biogeochemical processes in the sediment.

4.1. Early Diagenesis of Rhône Prodelta Sediments

The Rhône prodelta sediment is a highly dynamic environment in which flood-driven phenomena deliver considerable amounts of sedimentary materials that drive the biogeochemical characteristics of the zone. Integrating observed data with numerical modeling as done here can shed light on the different diagenetic processes that operate during periods of flood-induced organic matter input. However, this data-driven modeling approach can only be validated by the fidelity of the model in capturing the observed trend and variability present in the data. In this study, we provide some objective metrics to assess the skillfulness of the numerical model in reproducing the spatiotemporal pattern of the data set (Figure 3). Our findings demonstrate that the model porewater profiles for sulfate, DIC, iron, and manganese were well represented in both flood events in terms of their overall adjustment to the data and the variations with depth.

In contrast, despite their fair correlation with the data in the first 10 cm, the model skillfulness of the simulated results for manganese and iron at the initial state is less impressive. The vertical distribution of Mn and Fe porewater suggests a system in the process of slow evolution tightly coupled to other cycles (Figure 5). This could be related to the influence of previous limited floods (January and April 2008), which would still be in the relaxation process and not fully adjusted to the "average" forcings as simulated after the spin-up. With more data constraints for such evaluation (i.e., FeOx and MnOx deposition flux and reactivity), the model's performance could be improved through better characterization of the Fe dynamics. The lesser known dynamics and forcings (transient phases and OM lability) at the start of the perturbation, as well as the uncertainty about when this specific event occurred, may also be responsible for the bias in the May–June flood. Furthermore, our preliminary test carried with and without the inclusion of an intermediate flood deposition (around September) between the two events highlights the importance of data coverage and timescale of investigation for capturing the key features of the interstitial porewater signature arising from this type of event (Romans et al., 2016). In addition, the impact of the variable bio-irrigation rate for the different solutes can also have a profound effect on the modeled profiles and fluxes. Our experimentation showed that in reducing the bio-irrigation rate, the simulated fluxes were lowered in all dissolved species (results not shown). However, the porewater profiles simulated at this reduced irrigation rate is qualitatively less impressive than the reference irrigation rate employed here (Table 2). Furthermore, using a solute-specific irrigation rate have negligible difference in terms of simulated flux compared to the results presented here. Thus, from this ad hoc experiment, we note the trade-offs in fitting multicomponent reactive transport species in coastal sediment as well as the practical identifiability of true bio-irrigation coefficient profiles in the case of limited data (Meile et al., 2005), and more work is required to improve our representation of this process and better constrain Fe and Mn cycles in the region.

21699291, 2025, 6, Downloaded from https://agupubs.onlinelibrary.wiley.com/doi/10.1029/2025JC022414 by Universiteitsbibliotheek, Wiley Online Library on [07/01/2026]. See the Terms and Conditions (https://onlinelibrary.wiley.com/terms-and-conditions) on Wiley Online Library for rules of use; OA articles are governed by the applicable Creative Commons License

In terms of the benthic fluxes, sediment O_2 flux patterns have been measured in this region in 2008 and shows temporal variability linked to events of variable intensities (Cathalot et al., 2010). Our model O_2 flux (accounting for both diffusive and irrigative flux) in both flood events slightly overestimate the observed diffusive oxygen uptake (DOU) fluxes reported in Cathalot et al. (2010) and Pastor et al. (2018) for this particular prodelta site Figure 8. Upper values correspond to TOU already observed at this site (about 24 mmol C m^{-2} d^{-1}) (Lansard et al., 2008, 2009; Pastor et al., 2011a). This range of oxygen flux compared favorably to other RiOMar systems characterized by a high sedimentation rate and particulate organic carbon flux: Amazon Delta (6–25 mmol C m^{-2} d^{-1}; Aller et al. (1996)), Mississippi Delta (2–56 mmol C m^{-2} d^{-1}; Morse and Rowe (1999)), and other coastal areas with a pulse cycle of resuspension and deposition such as in Göteborg harbor, Sweden (8–23 mmol C m^{-2} d^{-1}; Tengberg et al. (2003)), Gulf of Finland, Baltic Sea (5–20 mmol C m^{-2} d^{-1}; Almroth et al. (2009)), and Gulf of Mexico (7–50 mmol C m^{-2} d^{-1}; Moriarty et al. (2018)).

Within the Rhône prodelta, the dynamical character of the porewater is closely coupled to the underlying transport and biogeochemical changes linked to massive depositional event. As in the case described in the fall flood, a strong oxygen consumption ensued in the first few days after the events via immediate degradation of organic carbon driven by oxic mineralization. Our model in agreement with the data showed substantial temporal variability in the O_2 flux driven by the variability in organic carbon input associated with the flood event. Especially, the lowering of O_2 fluxes observed after the spring flood is well represented by the model. Organic carbon mineralization in general was dominated by sulfate reduction in both spring and fall events. In both cases, the total mineralization increased by a factor of 1.5 in spring and 3 in fall (Figure 9) reflecting the amount and lability of the OM deposited—a much larger increase of the total carbon mineralization during the fall depositional event than the spring. During the spring event, a significant portion of the total mineralization was induced at the old sediment-water interface where a layer of degradable organic matter was buried by the flood deposit. This layer is located at 30 cm depth after the spring flood, therefore lowering the transfers at the present sediment-water interface. This organic-rich material fuels the intense subsurface sulfate reduction. Similar trapping and enhanced biogeochemical activities have also been reported in flooded organic-rich sediment in the Saguenay Fjord (Deflandre et al., 2002; Mucci et al., 2003).

This trend, however, was in contrast with the fall flood where the majority of the mineralization took place in the first 10 cm of the sediment, resulting from the deposition of organic-rich material during this flood. As a result of this dissimilar pattern, DIC production revealed that with organic-rich sediment deposition, particularly during the fall period, a strong DIC efflux across the sediment-water interface (up to 320 mmol DIC m^{-2} d^{-1}) can be expected. On the contrary in spring, recycling is internal (below the 30 cm flood layer), which should lead to reduced exchange with the water column (see below).

Short-term dynamics in manganese and iron redox cycling were assessed with the model constrained by the available data and empirical observations at this proximal site. The porewater chemistry in the prodelta was altered by the spring (generalized) and fall (Cevenol) floods, with contrasted responses for Mn and Fe. The model Mn oxides reduction rate was estimated around 16 mmol Mn m^{-2} d^{-1} in the spring compared to 31 mmol Mn m^{-2} d^{-1} in the fall. Chemical reduction by sulfide accounted for about 50% while microbially mediated reduction of organic carbon accounted for 49% during the spring deposition. The latter had a much lower contribution in fall (23%) than the spring event with a stronger contribution by Mn oxides reduction by H_2S. This fall enrichment of dissolved Mn in the upper sediment layer (up to 800 μM Figure 6) also seen in the Saguenay Fjord after a large depositional event (Deflandre et al., 2002) is driven by the strong imbalance between the sources and sinks (Table 4), resulting in its unique shape with the contribution from the MnO_2 reduction by H_2S as the major driver. In contrast, dissolved iron porewater profile is primarily controlled by the reductive dissolution of FeOOH by sulfides (68%). However, in the fall event, this large iron release is balanced in deeper layers by precipitation to a stable form of FeS and lost by burial to deeper layers. This dynamic diagenetic balance could be responsible for the peculiarity of the observed pattern of the dissolved iron profile (Figure 5). Indeed, other previous studies in the Rhône prodelta have alluded to this routing of iron sulfide precipitation as a possible mechanism for the maintenance of the observed ferruginous condition and the alkalinity fluxes (Pastor et al., 2018; Rassmann et al., 2020).

Furthermore, recent work by van de Velde et al. (2020) has demonstrated that oscillating redox circumstances can affect remineralization processes where a dominating Fe^{2+} state with regard to sulfide can occur due to the

21699291, 2025, 6, Downloaded from https://agupubs.onlinelibrary.wiley.com/doi/10.1029/2025JC022414 by Universiteitsbibliotheek, Wiley Online Library on [07/01/2026]. See the Terms and Conditions (https://onlinelibrary.wiley.com/terms-and-conditions) on Wiley Online Library for rules of use; OA articles are governed by the applicable Creative Commons License

sediment's inherent bistability. This bistability condition is determined by the ratio of particulate carbon to iron input. In our example, with significant carbon (Ait Ballagh et al., 2021; Pastor et al., 2011c) and iron flux (Marin & Giresse, 2001; Radakovitch et al., 2008; Roussiez et al., 2011), this ratio is 5, and such Fe-rich/sulfide-free condition is observed, as theoretically predicted by van de Velde et al. (2020) when combined with kinetically fast FeS formation as in the natural environment. Thus, our results highlight the suggested possibility of abiotic reduction of the metal oxides as well as precipitation of FeS (and subsequent pyrite formation) (Pastor et al., 2011c; Rassmann et al., 2020). These secondary reactions (especially abiotic reduction of manganese oxide by sulfide) may help explain the elevated Mn^{2+} concentration in the sediment after both floods with higher values in the fall (Pastor et al., 2018).

In general, the high metal reduction is a consequence of two factors: Firstly, the large deposition of terrigenous materials, which is linked to the high sedimentation rate and possibly large concentrations of reducible iron terrestrially transferred to this depocenter (Pastor et al., 2018; Roussiez et al., 2011). This is also implied by the higher α value imposed in November deposit in order to simulate such observed trend. The second factor is the highlighted role of secondary reactions in the diagenetic alteration of organic matter. This process involves the cycles of iron (Fe) and manganese (Mn), which are active and efficient in this region (Figure 7). These factors have been previously suggested to be responsible for the rapid recycling of manganese and iron in surface sediments (Rabouille & Gaillard, 1991; Van Cappellen & Wang, 1996; Wang & Van Cappellen, 1996). The second factor could be critical after flood deposition during the most dynamic part of a transiently changing system in maintaining the dominance of dissolved reduced metals in porewaters as observed in Figures 5 and 6 and the absence of $\sum H_2S$ in the porewater (Pastor et al., 2011c). This modeling insight into the role of the combined factor in the redox cycle of metals is also supported by observation in other dynamic sedimentary systems subject to episodic flood events (Blair & Aller, 2012).

4.2. Implication of Intense Flood Deposition in Biogeochemical Fluxes

As discussed previously, river-dominated margins serve as retention zones for riverine borne particulate matter and are subject to both anthropogenic and natural perturbations (Dai et al., 2022). Extreme flood events can bring large quantities of sediment within a short time frame, which has the possibility to induce changes in the biogeochemical properties of the sediment. In the Rhône River prodelta, the annual flood can deliver up to 5.4×10^6 tons of sediment in a 10-day period (Antonelli et al., 2008). This large volume of sediment delivered is also seen in similar river systems with rapid sedimentation of riverine materials: Pô River flood in 2007 (Miserocchi et al., 2007), Saguenay Fjord, Canada (landslide—Deflandre et al., 2002; Mucci & Edenborn, 1992). Thus, the introduction of these new materials can affect not only the carbon cycle but also the other elemental cycles such as iron and manganese as demonstrated in the previous sections.

Under a flood regime, biogeochemical processes undergo sudden change linked to biogeochemical conditions in the sediment. For example, the TOU rate initially decreases by 56% during the spring flood event and depending on the characteristics of the particulate input, strongly anoxic condition with greater propensity for methanogenesis can be induced. Our results (Figure 9) show that this is the case for pathways affecting the carbon cycle where sulfate reduction and methane production can be stimulated over short time intervals following massive sediment depositions. This decoupling of aerobic and anaerobic processes is rather unique to this particular site where the core incubation DIC:DOU ratio could be up to 7 and could lead to mismatch between DIC and diffusive oxygen fluxes (Rassmann et al., 2020). The substantial change in carbon mineralization results in enhanced DIC production and can have a considerable effect on DIC flux across the sediment-water interface. Our findings reveal that the intensity of DIC exchange varies with the flood type, with a much higher flux of DIC in the fall than the spring, reflecting the contrast in the thickness and nature of deposited materials.

Furthermore, the contrast in DIC flux simulated during these contrasted floods (Figure 8) indicates that different combinations of organic carbon mineralization and DIC transport mechanisms are at work in the deposited materials. Model simulations indicate that the spring deposition resulted in a decrease of the DIC flux after flood deposition, suggesting an internal production and porewater storage of the DIC, due to the mineralization of trapped reactive materials buried beneath the newly deposited refractory layer. On the contrary, mineralization of newly deposited labile OM in the fall resulted in a significant and rapid increase in DIC release in the flood layer and an increased exchange with the bottom water. These two contrasted responses demonstrate that different

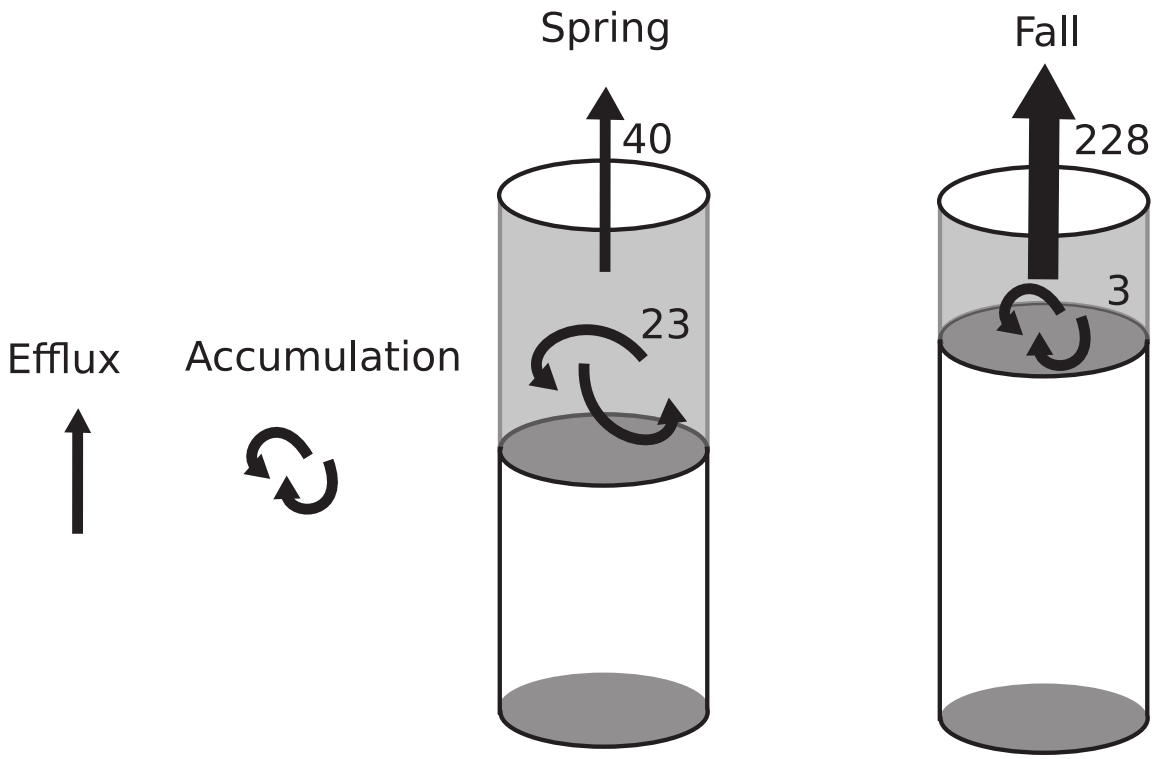

Figure 11. Synthesis of DIC dynamics for the spring (left) and fall (right) depositional events. The calculation is based on model outputs and integrated over the relaxation timescale (rts) of 4 months. The accumulation of DIC in the porewater was estimated by the change in inventory of DIC over the depth of the new deposit between the preflood time versus postflood time and divided by the relaxation time ($\Delta t_{\mathrm{rts}} = 4$ months) that is, $\frac{1}{\Delta t_{\mathrm{rts}}}\left(\int_0^{\mathrm{zpert}} C(t_{\mathrm{event}+\mathrm{rts}})\,dz - \int_0^{\mathrm{zpert}} C(t_{\mathrm{event}})\,dz\right)$. The DIC flux out of the sediment was calculated using model result in Section 3.3.1 integrated and averaged over the relaxation timescale that is, $\frac{1}{\Delta_{\mathrm{rts}}}\int_{t_{\mathrm{event}}}^{t_{\mathrm{event}+\mathrm{rst}}} \mathrm{DIC}_{\mathrm{flux}}\,dt$. All units are in mmol m^{-2} d^{-1}.

types of floods might have a diverse influence on material exchange with the water column, which has a considerable impact on coastal carbon dynamics (Bauer et al., 2013; Cai, 2011).

We can appreciate this differential response of the coastal sediment to episodic carbon input of contrasted thickness and lability by comparing the different fluxes constituting the mass balance as calculated by the model (accumulation in porewaters and flux at the sediment-water interface) over the time span of DIC relaxation (~4 months; (Nmor et al., 2022)). Figure 11 indicates that during the spring flood, DIC flux out of the sediment integrated and averaged over 4 months was 40 mmol m^{-2} d^{-1} whereas in that same time frame, about 23 mmol m^{-2} d^{-1} of DIC accumulated in the sediment interior driven by diffusion from below in the more refractory flood layer. This amounts to a DIC efflux/accumulation ratio of 2 in the spring. In contrast, the fall deposition presented a different picture with a higher efflux to the accumulation ratio of about 78 (228/3) related to the intense mineralization of labile and organic-rich flood layer near the sediment-water interface.

In addition, massive sediment deposition can also trigger changes in metal recycling efficiency of the sediment. This can result in a diagenetic response of iron and manganese, which has consequences on the long-term fate of their respective cycle. For example, metal reduction during nonsteady state condition has been shown to be a source of dissolved organic carbon (Deflandre et al., 2002). Furthermore, some of the reduced Fe within the sediment column is sequestered with sulfides, which can be critical for the perennial burial of sulfur in the sediment (Jørgensen et al., 2019). This might be the case in deltaic systems connected to river mouths, which are dominated by anoxic diagenesis, with intense sulfate and iron oxide reduction, as this can lead to the precipitation and burial of FeS/FeS_2 (Aller et al., 1996). This is actually the scenario for the Rhône prodelta sediment where the precipitation of particulate FeS (FeS_p) has been detected and is linked to a large alkalinity release (Rassmann et al., 2020). Flood inputs can deeply modify the internal Fe/S cycling, favor FeS production, and contribute to reduced species burial, thus controlling alkalinity fluxes to the water column (Rassmann et al., 2020).

21699291, 2025, 6, Downloaded from https://agupubs.onlinelibrary.wiley.com/doi/10.1029/2025JC022414 by Universiteitsbibliotheek, Wiley Online Library on [07/01/2026]. See the Terms and Conditions (https://onlinelibrary.wiley.com/terms-and-conditions) on Wiley Online Library for rules of use; OA articles are governed by the applicable Creative Commons License

21699291, 2025, 6, Downloaded from https://agupubs.onlinelibrary.wiley.com/doi/10.1029/2025JC022414 by Universiteitsbibliotheek, Wiley Online Library on [07/01/2026]. See the Terms and Conditions (https://onlinelibrary.wiley.com/terms-and-conditions) on Wiley Online Library for rules of use; OA articles are governed by the applicable Creative Commons License

4.3. Interaction Between Successive Floods

As our understanding of rapidly accumulating sedimentary systems continues to improve as a result of better observing systems (Maillet et al., 2006; Toussaint et al., 2014; Viollier et al., 2003; Zebracki et al., 2015) and greater appreciation for transient benthic biogeochemical processes (Cathalot et al., 2010; Mucci et al., 2003; Nmor et al., 2022; Pastor et al., 2018; Tesi et al., 2012), the influence of successive depositions of OM materials via these extreme flood events needs to be investigated. One widely recognized consequence of this phenomenon is the decoupling of oxygen consumption from carbon mineralization during transient flood condition (Aller, 1998; Rassmann et al., 2020). Another ramification of this back-to-back occurrence of flood deposition is the cumulative impact induced on the biogeochemical processes. This is demonstrated in our experimental simulation (Figure 10) where the cooccurrence of sequential flood deposition initiates a temporal lag in the carbon mineralization pathways. Interestingly, the memory effect is visible only for the slow relaxing species (methane and sulfate). As such, biogeochemical species associated with anaerobic processes (methanogenesis and sulfate reduction) have a larger memory effect brought forth by the sediment deposition. This might be the case where the activities involving these pathways take place significantly deeper in the sediment generating a longer relaxation time dictated by their longer diffusive time (Nmor et al., 2022). In this regard, methanogenesis, which has the largest relaxation time, also shows the largest memory effect (38%). This is clearly a cumulative effect from the first flood to the second flood as methanogenesis is around 4 times larger at the start of the second flood than the initial preflood state.

However, this link between successive flood deposition and cumulative impact of diagenetic cycling of organic carbon is not entirely positive for all OC degradation pathways (i.e., sequential deposition of new sediment materials does not always relate to significant biogeochemical imprint of past flood input). We see in the case of sulfate, for example, where negative memory effect can arise. While it is not entirely clear what mechanism is responsible for this effect, one possibility could be attributed to the greater intensification of sulfate reduction following the introduction of OM-rich sediment during the fall deposition. The existence of this reactive OC in this fall-only scenario causes the system to favor sulfate reduction as the principal pathway for OM mineralization, as opposed to the spring + fall scenario, where sulfate reduction contributes 10% less. Indeed, the relationship between flood input parameters (thickness, OM lability), flood event frequency, and sediment biogeochemical changes is complicated and tightly coupled.

In general, results here show that episodic events such as those observed in the Rhône prodelta and other similar regions can lead to transient states within a perturbation window of a few months (2–6 months) (van de Velde et al., 2018) and in the occurrence of multiple events, stimulate enhanced anoxic mineralization of carbon. Recent flood event in the western Mediterranean indicates the recurrent nature of these types of episodic flood event similar (Ferreira et al., 2024) as fall winter floods are a major feature of this geographical area (Zebracki et al., 2015). Further investigation on the role of this flood-modulated interaction should be conducted to ascertain the biogeochemical implication of this phenomenon especially on a longer timescale.

5. Conclusion

Floods in the river-ocean continuum can deposit sediment materials of several tens of centimeters in a short period of time. As particulate OM is tightly coupled to carbon mineralization in the Rhône River prodelta sediment, this study focuses on two unique flood depositions with variable sediment characteristics (thick organic-poor in spring and thin organic-rich in fall), resulting in distinct biogeochemical responses. The labile nature of the OM provided during the 2008 fall season led to a much higher increase in organic carbon mineralization than the spring flood. The diagenetic pathway supporting this OC mineralization increase was mostly sulfate reduction as indicated by changes in porewater profiles of sulfate and DIC between the two floods. The different nature of the two floods induced opposite effects on DIC release from sediments with burst of DIC release in the fall versus a decrease of DIC efflux in spring. This highlights the importance of internal versus near-surface recycling of carbon in controlling the solute exchange across the SWI. Despite substantial sulfate reduction, no dissolved sulfide was detected in the porewater, perhaps indicating strong precipitation with Fe and H_2S-mediated reduction of manganese and iron oxides. The model supporting this paradigm emphasizes the involvement of secondary redox mechanisms (representing >75% of metal reduction) in sustaining the observed profiles in both flood situations. In addition, the sequential accumulation of sediment can also trigger an interaction between two independent flood depositions if the frequency of their occurrence is high enough to cause an overlap between them. In this

21699291, 2025, 6, Downloaded from https://agupubs.onlinelibrary.wiley.com/doi/10.1029/2025JC022414 by Universitetsbiblioteket, Wiley Online Library on [07/01/2026]. See the Terms and Conditions (https://onlinelibrary.wiley.com/terms-and-conditions) on Wiley Online Library for rules of use; OA articles are governed by the applicable Creative Commons License

case, we demonstrated that anoxic mineralization processes such as sulfate reduction and, in particular, methanogenesis can be influenced by this consecutive flood if it occurs more frequently in the future.

Data Availability Statement

The data used in this study can be retrieved from Pastor et al. (2018) and can be downloaded from https://doi.org/10.5281/zenodo.6369288. The FESDIA model code used to generate the simulation is openly available in https://doi.org/10.5281/zenodo.15480112 and can also be obtained via https://github.com/stanleesocca/GMD-FESDIA/tree/v1.1.0.

Acknowledgments
This research has been supported by a grant from INSU EC2C0 DELTARhône, by the PPR-RiOMar project, a French government grant managed by the Agence Nationale de la Recherche under the France 2030 program, reference ANR 22 POCE 0006, and a PhD grant from Ecole doctorale des Sciences de l'Environment, Ile de France (SEIF) N° 129.

References

Ait Ballagh, F. E., Rabouille, C., Andrieux-Loyer, F., Soetaert, K., Lansard, B., Bombled, B., et al. (2021). Spatial variability of organic matter and phosphorus cycling in Rhône river prodelta sediments (NW Mediterranean Sea, France): A model-data approach. *Estuaries and Coasts*, *44*(7), 1765–1789. https://doi.org/10.1007/s12237-020-00889-9

Aller, R., Blair, N., Xia, Q., & Rude, P. (1996). Remineralization rates, recycling, and storage of carbon in amazon shelf sediments. *Continental Shelf Research*, *16*(5–6), 753–786. https://doi.org/10.1016/0278-4343(95)00046-1

Aller, R. C. (1980). Diagenetic processes near the sediment-water interface of long island sound. I.: Decomposition and nutrient element geochemistry (s, n, p). In *Advances in geophysics* (Vol. 22, pp. 237–350). Elsevier. https://doi.org/10.1016/s0065-2687(08)60067-9

Aller, R. C. (1998). Mobile deltaic and continental shelf muds as suboxic, fluidized bed reactors. *Marine Chemistry*, *61*(3–4), 143–155. https://doi.org/10.1016/s0304-4203(98)00024-3

Allison, M. A., Lee, M. T., Ogston, A. S., & Aller, R. C. (2000). Origin of amazon mudbanks along the northeastern coast of south America. *Marine Geology*, *163*(1–4), 241–256. https://doi.org/10.1016/s0025-3227(99)00120-6

Almroth, E., Tengberg, A., Andersson, J. H., Pakhomova, S., & Hall, P. O. (2009). Effects of resuspension on benthic fluxes of oxygen, nutrients, dissolved inorganic carbon, iron and manganese in the gulf of Finland, Baltic Sea. *Continental Shelf Research*, *29*(5–6), 807–818. https://doi.org/10.1016/j.csr.2008.12.011

Antonelli, C., Eyrolle, F., Rolland, B., Provansal, M., & Sabatier, F. (2008). Suspended sediment and 137Cs fluxes during the exceptional December 2003 flood in the Rhone River, southeast France. *Geomorphology*, *95*(3–4), 350–360. https://doi.org/10.1016/j.geomorph.2007.06.007

Bao, R., Zhao, M., McNichol, A., Wu, Y., Guo, X., Haghipour, N., & Eglinton, T. I. (2019). On the origin of aged sedimentary organic matter along a river-shelf-deep ocean transect. *Journal of Geophysical Research: Biogeosciences*, *124*(8), 2582–2594. https://doi.org/10.1029/2019jg005107

Bauer, J. E., Cai, W.-J., Raymond, P. A., Bianchi, T. S., Hopkinson, C. S., & Regnier, P. A. (2013). The changing carbon cycle of the coastal ocean. *Nature*, *504*(7478), 61–70. https://doi.org/10.1038/nature12857

Bentley, S. J., & Nittrouer, C. A. (2003). Emplacement, modification, and preservation of event strata on a flood-dominated continental shelf: Eel shelf, northern California. *Continental Shelf Research*, *23*(16), 1465–1493. https://doi.org/10.1016/j.csr.2003.08.005

Berg, P., Rysgaard, S., & Thamdrup, B. (2003). Dynamic modeling of early diagenesis and nutrient cycling. A case study in an artic marine sediment. *American Journal of Science*, *303*(10), 905–955. https://doi.org/10.2475/ajs.303.10.905

Bianucci, L., Balaguru, K., Smith, R. W., Leung, L. R., & Moriarty, J. M. (2018). Contribution of hurricane-induced sediment resuspension to coastal oxygen dynamics. *Scientific Reports*, *8*(1), 1–10. https://doi.org/10.1038/s41598-018-33640-3

Blair, N. E., & Aller, R. C. (2012). The fate of terrestrial organic carbon in the marine environment. *Annual Review of Marine Science*, *4*(1), 401–423. https://doi.org/10.1146/annurev-marine-120709-142717

Bonifácio, P., Bourgeois, S., Labrune, C., Amouroux, J. M., Escoubeyrou, K., Buscail, R., et al. (2014). Spatiotemporal changes in surface sediment characteristics and benthic macrofauna composition off the Rhône River in relation to its hydrological regime. *Estuarine, Coastal and Shelf Science*, *151*, 196–209. https://doi.org/10.1016/j.ecss.2014.10.011

Bourgeois, S., Pruski, A., Sun, M.-Y., Buscail, R., Lantoine, F., Kerhervé, P., et al. (2011). Distribution and lability of land-derived organic matter in the surface sediments of the Rhône prodelta and the adjacent shelf (Mediterranean Sea, France): A multi proxy study. *Biogeosciences*, *8*(11), 3107–3125. https://doi.org/10.5194/bg-8-3107-2011

Bourrin, F., Friend, P. L., Amos, C. L., Manca, E., Ulses, C., Palanques, A., et al. (2008). Sediment dispersal from a typical Mediterranean flood: The Têt River, Gulf of Lions. *Continental Shelf Research*, *28*(15), 1895–1910. https://doi.org/10.1016/j.csr.2008.06.005

Burdige, D. J. (1993). The biogeochemistry of manganese and iron reduction in marine sediments. *Earth-Science Reviews*, *35*(3), 249–284. https://doi.org/10.1016/0012-8252(93)90040-e

Burdige, D. J. (2005). Burial of terrestrial organic matter in marine sediments: A re-assessment. *Global Biogeochemical Cycles*, *19*(4). https://doi.org/10.1029/2004gb002368

Cai, W.-J. (2011). Estuarine and coastal ocean carbon paradox: CO_2 sinks or sites of terrestrial carbon incineration? *Annual Review of Marine Science*, *3*(1), 123–145. https://doi.org/10.1146/annurev-marine-120709-142723

Canfield, D. E., Raiswell, R., & Bottrell, S. H. (1992). The reactivity of sedimentary iron minerals toward sulfide. *American Journal of Science*, *292*(9), 659–683. https://doi.org/10.2475/001c.60600

Carter, R., Larcombe, P., Dye, J., Gagan, M., & Johnson, D. (2009). Long-shelf sediment transport and storm-bed formation by cyclone Winifred, central Great Barrier Reef, Australia. *Marine Geology*, *267*(3–4), 101–113. https://doi.org/10.1016/j.margeo.2009.08.009

Cathalot, C., Rabouille, C., Pastor, L., Deflandre, B., Viollier, E., Buscail, R., et al. (2010). Temporal variability of carbon recycling in coastal sediments influenced by rivers: Assessing the impact of flood inputs in the Rhône River prodelta. *Biogeosciences*, *7*(3), 1187–1205. https://doi.org/10.5194/bg-7-1187-2010

Cathalot, C., Rabouille, C., Tisnérat-Laborde, N., Toussaint, F., Kerhervé, P., Buscail, R., et al. (2013). The fate of river organic carbon in coastal areas: A study in the Rhône River delta using multiple isotopic ($\delta^{13}C$, $\Delta^{14}C$) and organic tracers. *Geochimica et Cosmochimica Acta*, *118*, 33–55. https://doi.org/10.1016/j.gca.2013.05.001

Chakrapani, G. J. (2005). Factors controlling variations in river sediment loads. *Current Science*, 569–575.

Charmasson, S., Radakovitch, O., Arnaud, M., Bouisset, P., & Pruchon, A.-S. (1998). Long-core profiles of 137 CS, 134 CS, 60 co and 210 pb in sediment near the Rhone River (northwestern Mediterranean Sea). *Estuaries*, *21*(3), 367–378. https://doi.org/10.2307/1352836

Cheng, P., Li, M., & Li, Y. (2013). Generation of an estuarine sediment plume by a tropical storm. *Journal of Geophysical Research: Oceans*, *118*(2), 856–868. https://doi.org/10.1002/jgrc.20070

Copard, Y., Eyrolle, F., Radakovitch, O., Poirel, A., Raimbault, P., Gairoard, S., & Di-Giovanni, C. (2018). Badlands as a hot spot of petrogenic contribution to riverine particulate organic carbon to the Gulf of Lion (NW Mediterranean Sea). *Earth Surface Processes and Landforms*, *43*(12), 2495–2509. https://doi.org/10.1002/esp.4409

Dai, M., Su, J., Zhao, Y., Hofmann, E. E., Cao, Z., Cai, W. J., et al. (2022). Carbon fluxes in the coastal ocean: Synthesis, boundary processes, and future trends. *Annual Review of Earth and Planetary Sciences*, *50*(1), 593–626. https://doi.org/10.1146/annurev-earth-032320-090746

Dale, A. W., Nickelsen, L., Scholz, F., Hensen, C., Oschlies, A., & Wallmann, K. (2015). A revised global estimate of dissolved iron fluxes from marine sediments. *Global Biogeochemical Cycles*, *29*(5), 691–707. https://doi.org/10.1002/2014gb005017

Dale, A. W., Regnier, P., & Van Cappellen, P. (2006). Bioenergetic controls on anaerobic oxidation of methane (AOM) in coastal marine sediments: A theoretical analysis. *American Journal of Science*, *306*(4), 246–294. https://doi.org/10.2475/ajs.306.4.246

Deflandre, B., Mucci, A., Gagné, J.-P., Guignard, C., & jørn Sundby, B. (2002). Early diagenetic processes in coastal marine sediments disturbed by a catastrophic sedimentation event. *Geochimica et Cosmochimica Acta*, *66*(14), 2547–2558. https://doi.org/10.1016/s0016-7037(02)00861-x

Dufois, F., Verney, R., Le Hir, P., Dumas, F., & Charmasson, S. (2014). Impact of winter storms on sediment erosion in the Rhone river prodelta and fate of sediment in the gulf of lions (north western Mediterranean Sea). *Continental Shelf Research*, *72*, 57–72. https://doi.org/10.1016/j.csr.2013.11.004

Estournel, C., Mikolajczak, G., Ulses, C., Bourrin, F., Canals, M., Charmasson, S., et al. (2023). Sediment dynamics in the gulf of lion (NW Mediterranean Sea) during two autumn–winter periods with contrasting meteorological conditions. *Progress in Oceanography*, *210*, 102942. https://doi.org/10.1016/j.pocean.2022.102942

Eyrolle, F., Radakovitch, O., Raimbault, P., Charmasson, S., Antonelli, C., Ferrand, E., et al. (2012). Consequences of hydrological events on the delivery of suspended sediment and associated radionuclides from the Rhône River to the Mediterranean Sea. *Journal of Soils and Sediments*, *12*(9), 1479–1495. https://doi.org/10.1007/s11368-012-0575-0

Ferreira, E., Nmor, S., Viollier, E., Lansard, B., Bombled, B., Regnier, E., et al. (2024). Characterization of the benthic biogeochemical dynamics after flood events in the Rhône River prodelta: A data–model approach. *Biogeosciences*, *21*(3), 711–729. https://doi.org/10.5194/bg-21-711-2024

Froelich, P. N., Klinkhammer, G. P., Bender, M. L., Luedtke, N. A., Heath, G. R., Cullen, D., et al. (1979). Early oxidation of organic matter in pelagic sediments of the eastern equatorial Atlantic: Suboxic diagenesis. *Geochimica et Cosmochimica Acta*, *43*(7), 1075–1090. https://doi.org/10.1016/0016-7037(79)90095-4

Haese, R. R. (2000). The reactivity of iron, in marine geochemistry. In H. D. Schulz (Ed.), *Marine geochemistry* (pp. 233–261). Springer.

Jørgensen, B. B., Findlay, A. J., & Pellerin, A. (2019). The biogeochemical sulfur cycle of marine sediments. *Frontiers in Microbiology*, *10*, 849. https://doi.org/10.3389/fmicb.2019.00849

Lansard, B., Rabouille, C., Denis, L., & Grenz, C. (2008). In situ oxygen uptake rates by coastal sediments under the influence of the Rhône River (NW Mediterranean Sea). *Continental Shelf Research*, *28*(12), 1501–1510. https://doi.org/10.1016/j.csr.2007.10.010

Lansard, B., Rabouille, C., Denis, L., & Grenz, C. (2009). Benthic remineralization at the land–ocean interface: A case study of the Rhône River (NW Mediterranean Sea). *Estuarine, Coastal and Shelf Science*, *81*(4), 544–554. https://doi.org/10.1016/j.ecss.2008.11.025

LaRowe, D. E., Arndt, S., Bradley, J., Estes, E., Hoarfrost, A., Lang, S., et al. (2020). The fate of organic carbon in marine sediments-new insights from recent data and analysis. *Earth-Science Reviews*, *204*, 103146. https://doi.org/10.1016/j.earscirev.2020.103146

Mackenzie, F., Lerman, A., & Andersson, A. (2004). Past and present of sediment and carbon biogeochemical cycling models. *Biogeosciences*, *1*(1), 11–32. https://doi.org/10.5194/bg-1-11-2004

Maillet, G. M., Vella, C., Berné, S., Friend, P. L., Amos, C. L., Fleury, T. J., & Normand, A. (2006). Morphological changes and sedimentary processes induced by the December 2003 flood event at the present mouth of the grand Rhône River (southern France). *Marine Geology*, *234*(1–4), 159–177.

Marin, B., & Giresse, P. (2001). Particulate manganese and iron in recent sediments of the Gulf of Lions continental margin (north-western Mediterranean Sea): Deposition and diagenetic process. *Marine Geology*, *172*(1–2), 147–165. https://doi.org/10.1016/s0025-3227(00)00124-9

Marion, C., Dufois, F., Arnaud, M., & Vella, C. (2010). In situ record of sedimentary processes near the Rhône river mouth during winter events (Gulf of Lions, Mediterranean Sea). *Continental Shelf Research*, *30*(9), 1095–1107. https://doi.org/10.1016/j.csr.2010.02.015

McKee, B. A., Aller, R., Allison, M., Bianchi, T., & Kineke, G. (2004). Transport and transformation of dissolved and particulate materials on continental margins influenced by major rivers: Benthic boundary layer and seabed processes. *Continental Shelf Research*, *24*(7–8), 899–926. https://doi.org/10.1016/j.csr.2004.02.009

Meile, C., Berg, P., Van Cappellen, P., & Tuncay, K. (2005). Solute-specific pore water irrigation: Implications for chemical cycling in early diagenesis. *Journal of Marine Research*, *63*(3), 601–621. https://doi.org/10.1357/0022240054307885

Miserocchi, S., Langone, L., & Tesi, T. (2007). Content and isotopic composition of organic carbon within a flood layer in the Po river prodelta (Adriatic Sea). *Continental Shelf Research*, *27*(3–4), 338–358. https://doi.org/10.1016/j.csr.2005.05.005

Montanher, O. C., de Novo, E. M. L. M., & de Souza Filho, E. E. (2018). Temporal trend of the suspended sediment transport of the Amazon River (1984–2016). *Hydrological Sciences Journal*, *63*(13–14), 1901–1912. https://doi.org/10.1080/02626667.2018.1546387

Moriarty, J. M., Friedrichs, M. A., & Harris, C. K. (2021). Seabed resuspension in the Chesapeake Bay: Implications for biogeochemical cycling and hypoxia. *Estuaries and Coasts*, *44*(1), 103–122. https://doi.org/10.1007/s12237-020-00763-8

Moriarty, J. M., Harris, C. K., Friedrichs, M. A., Fennel, K., & Xu, K. (2018). Impact of seabed resuspension on oxygen and nitrogen dynamics in the northern Gulf of Mexico: A numerical modeling study. *Journal of Geophysical Research: Oceans*, *123*(10), 7237–7263. https://doi.org/10.1029/2018jc013950

Morse, J. W., & Rowe, G. T. (1999). Benthic biogeochemistry beneath the Mississippi River plume. *Estuaries*, *22*(2), 206–214. https://doi.org/10.2307/1352977

Mucci, A., Boudreau, B., & Guignard, C. (2003). Diagenetic mobility of trace elements in sediments covered by a flash flood deposit: Mn, Fe and As. *Applied Geochemistry*, *18*(7), 1011–1026. https://doi.org/10.1016/s0883-2927(02)00207-x

Mucci, A., & Edenborn, H. M. (1992). Influence of an organic-poor landslide deposit on the early diagenesis of iron and manganese in a coastal marine sediment. *Geochimica et Cosmochimica Acta*, *56*(11), 3909–3921. https://doi.org/10.1016/0016-7037(92)90005-4

Nmor, S. I., Viollier, E., Pastor, L., Lansard, B., Rabouille, C., & Soetaert, K. (2022). FESDIA (v1. 0): Exploring temporal variations of sediment biogeochemistry under the influence of flood events using numerical modelling. *Geoscientific Model Development*, *15*(19), 7325–7351. https://doi.org/10.5194/gmd-15-7325-2022

Osburn, C. L., Rudolph, J. C., Paerl, H. W., Hounshell, A. G., & Van Dam, B. R. (2019). Lingering carbon cycle effects of hurricane Matthew in North Carolina's coastal waters. *Geophysical Research Letters*, *46*(5), 2654–2661. https://doi.org/10.1029/2019gl082014

21699291, 2025, 6, Downloaded from https://agupubs.onlinelibrary.wiley.com/doi/10.1029/2025JC022414 by Universitetsbiblioteket, Wiley Online Library on [07/01/2026]. See the Terms and Conditions (https://onlinelibrary.wiley.com/terms-and-conditions) on Wiley Online Library for rules of use; OA articles are governed by the applicable Creative Commons License

Palinkas, C., Nittrouer, C., Wheatcroft, R., & Langone, L. (2005). The use of 7Be to identify event and seasonal sedimentation near the Po River delta, Adriatic Sea. *Marine Geology*, *222*, 95–112. https://doi.org/10.1016/j.margeo.2005.06.011

Pastor, L., Cathalot, C., Deflandre, B., Viollier, E., Soetaert, K., Meysman, F., et al. (2011b). Modeling biogeochemical processes in sediments from the Rhône river prodelta area (NW Mediterranean Sea). *Biogeosciences*, *8*(5), 1351–1366. https://doi.org/10.5194/bg-8-1351-2011

Pastor, L., Cathalot, C., Deflandre, B., Viollier, E., Soetaert, K., Meysman, F. J. R., et al. (2011c). Modeling biogeochemical processes in sediments from the Rhône River prodelta area (NW Mediterranean Sea). *Biogeosciences*, *8*(5), 1351–1366. https://doi.org/10.5194/bg-8-1351-2011

Pastor, L., Deflandre, B., Viollier, E., Cathalot, C., Metzger, E., Rabouille, C., et al. (2011a). Influence of the organic matter composition on benthic oxygen demand in the Rhône river prodelta (NW Mediterranean Sea). *Continental Shelf Research*, *31*(9), 1008–1019. https://doi.org/10.1016/j.csr.2011.03.007

Pastor, L., Rabouille, C., Metzger, E., Thibault de Chanvalon, A., Viollier, E., & Deflandre, B. (2018). Transient early diagenetic processes in Rhône prodelta sediments revealed in contrasting flood events. *Continental Shelf Research*, *166*, 65–76. https://doi.org/10.1016/j.csr.2018.07.005

Pont, D., Day, J. W., & Ibáñez, C. (2017). The impact of two large floods (1993–1994) on sediment deposition in the Rhône delta: Implications for sustainable management. *The Science of the Total Environment*, *609*, 251–262. https://doi.org/10.1016/j.scitotenv.2017.07.155

Pont, D., Simonnet, J.-P., & Walter, A.-V. (2002). Medium-term changes in suspended sediment delivery to the ocean: Consequences of catchment heterogeneity and river management (Rhône river, France). *Estuarine, Coastal and Shelf Science*, *54*(1), 1–18. https://doi.org/10.1006/ecss.2001.0829

Poulton, S., & Raiswell, R. (2002). The low-temperature geochemical cycle of iron: From continental fluxes to marine sediment deposition. *American Journal of Science*, *302*(9), 774–805. https://doi.org/10.2475/ajs.302.9.774

Poulton, S. W., Krom, M. D., & Raiswell, R. (2004). A revised scheme for the reactivity of iron (oxyhydr) oxide minerals towards dissolved sulfide. *Geochimica et Cosmochimica Acta*, *68*(18), 3703–3715. https://doi.org/10.1016/j.gca.2004.03.012

Pruski, A. M., Buscail, R., Bourgeois, S., Vétion, G., Coston-Guarini, J., & Rabouille, C. (2015). Biogeochemistry of fatty acids in a river-dominated Mediterranean ecosystem (Rhône river prodelta, Gulf of Lions, France): Origins and diagenesis. *Organic Geochemistry*, *83*, 227–240.

Rabouille, C., & Gaillard, J.-F. (1991). Towards the EDGE: Early diagenetic global explanation. A model depicting the early diagenesis of organic matter, O_2, NO_3, Mn, and PO_4. *Geochimica et Cosmochimica Acta*, *55*(9), 2511–2525. https://doi.org/10.1016/0016-7037(91)90369-g

Radakovitch, O., Roussiez, V., Ollivier, P., Ludwig, W., Grenz, C., & Probst, J.-L. (2008). Input of particulate heavy metals from rivers and associated sedimentary deposits on the gulf of lion continental shelf. *Estuarine, Coastal and Shelf Science*, *77*(2), 285–295. https://doi.org/10.1016/j.ecss.2007.09.028

Raiswell, R., & Canfield, D. E. (1998). Sources of iron for pyrite formation in marine sediments. *American Journal of Science*, *298*(3), 219–245. https://doi.org/10.2475/ajs.298.3.219

Rassmann, J., Eitel, E. M., Lansard, B., Cathalot, C., Brandily, C., Taillefert, M., & Rabouille, C. (2020). Benthic alkalinity and dissolved inorganic carbon fluxes in the Rhône River prodelta generated by decoupled aerobic and anaerobic processes. *Biogeosciences*, *17*(1), 13–33. https://doi.org/10.5194/bg-17-13-2020

Rassmann, J., Lansard, B., Pozzato, L., & Rabouille, C. (2016). Carbonate chemistry in sediment porewaters of the Rhône river delta driven by early diagenesis (northwestern Mediterranean). *Biogeosciences*, *13*(18), 5379–5394. https://doi.org/10.5194/bg-13-5379-2016

Regnier, P., Resplandy, L., Najjar, R. G., & Ciais, P. (2022). The land-to-ocean loops of the global carbon cycle. *Nature*, *603*(7901), 401–410. https://doi.org/10.1038/s41586-021-04339-9

Rickard, D. (1997). Kinetics of pyrite formation by the H2S oxidation of iron (II) monosulfide in aqueous solutions between 25 and 125 C: The rate equation. *Geochimica et Cosmochimica Acta*, *61*(1), 115–134. https://doi.org/10.1016/s0016-7037(96)00321-3

Rickard, D. (2006). The solubility of FeS. *Geochimica et Cosmochimica Acta*, *70*(23), 5779–5789. https://doi.org/10.1016/j.gca.2006.02.029

Romans, B. W., Castelltort, S., Covault, J. A., Fildani, A., & Walsh, J. (2016). Environmental signal propagation in sedimentary systems across timescales. *Earth-Science Reviews*, *153*, 7–29. https://doi.org/10.1016/j.earscirev.2015.07.012

Roussiez, V., Ludwig, W., Radakovitch, O., Probst, J.-L., Monaco, A., Charrière, B., & Buscail, R. (2011). Fate of metals in coastal sediments of a Mediterranean flood-dominated system: An approach based on total and labile fractions. *Estuarine, Coastal and Shelf Science*, *92*(3), 486–495. https://doi.org/10.1016/j.ecss.2011.02.009

Soetaert, K., Herman, P. M., & Middelburg, J. J. (1996). A model of early diagenetic processes from the shelf to abyssal depths. *Geochimica et Cosmochimica Acta*, *60*(6), 1019–1040. https://doi.org/10.1016/0016-7037(96)00013-0

Soetaert, K., & Petzoldt, T. (2010). Inverse modelling, sensitivity and Monte Carlo analysis in r using package FME. *Journal of Statistical Software*, *33*(3), 1–28. https://doi.org/10.18637/jss.v033.i03

Taylor, K. E. (2001). Summarizing multiple aspects of model performance in a single diagram. *Journal of Geophysical Research*, *106*(D7), 7183–7192. https://doi.org/10.1029/2000jd900719

Tegler, L. A., Horner, T. J., Galy, V., Bent, S. M., Wang, Y., Kim, H. H., et al. (2024). Distribution and drivers of organic carbon sedimentation along the continental margins. *AGU Advances*, *5*(4), e2023AV001000. https://doi.org/10.1029/2023av001000

Tengberg, A., Almroth, E., & Hall, P. (2003). Resuspension and its effects on organic carbon recycling and nutrient exchange in coastal sediments: In situ measurements using new experimental technology. *Journal of Experimental Marine Biology and Ecology*, *285*, 119–142. https://doi.org/10.1016/s0022-0981(02)00523-3

Tesi, T., Langone, L., Goñi, M., Wheatcroft, R., Miserocchi, S., & Bertotti, L. (2012). Early diagenesis of recently deposited organic matter: A 9-yr time-series study of a flood deposit. *Geochimica et Cosmochimica Acta*, *83*, 19–36. https://doi.org/10.1016/j.gca.2011.12.026

Tesi, T., Miserocchi, S., Acri, F., Langone, L., Boldrin, A., Hatten, J., & Albertazzi, S. (2013). Flood-driven transport of sediment, particulate organic matter, and nutrients from the Po river watershed to the Mediterranean Sea. *Journal of Hydrology*, *498*, 144–152. https://doi.org/10.1016/j.jhydrol.2013.06.001

Thamdrup, B. (2000). Bacterial manganese and iron reduction in aquatic sediments. *Advances in Microbial Ecology*, 41–84. https://doi.org/10.1007/978-1-4615-4187-5_2

Tockner, K., & Stanford, J. A. (2002). Riverine flood plains: Present state and future trends. *Environmental Conservation*, *29*(3), 308–330. https://doi.org/10.1017/s037689290200022x

Toussaint, F., Rabouille, C., Cathalot, C., Bombled, B., Abchiche, A., Aouji, O., et al. (2014). A new device to follow temporal variations of oxygen demand in deltaic sediments: The LSCE benthic station. *Limnology and Oceanography: Methods*, *12*(11), 729–741. https://doi.org/10.4319/lom.2014.12.729

Ulses, C., Estournel, C., De Madron, X. D., & Palanques, A. (2008). Suspended sediment transport in the Gulf of Lions (NW Mediterranean): Impact of extreme storms and floods. *Continental Shelf Research*, *28*(15), 2048–2070. https://doi.org/10.1016/j.csr.2008.01.015

21699291, 2025, 6, Downloaded from https://agupubs.onlinelibrary.wiley.com/doi/10.1029/2025JC022414 by Universitetsbiblioteket, Wiley Online Library on [07/01/2026]. See the Terms and Conditions (https://onlinelibrary.wiley.com/terms-and-conditions) on Wiley Online Library for rules of use; OA articles are governed by the applicable Creative Commons License

Van Cappellen, P., & Wang, Y. (1996). Cycling of iron and manganese in surface sediments; a general theory for the coupled transport and reaction of carbon, oxygen, nitrogen, sulfur, iron, and manganese. *American Journal of Science*, *296*(3), 197–243. https://doi.org/10.2475/ajs.296.3.197

van de Velde, S., & Meysman, F. J. (2016). The influence of bioturbation on iron and sulphur cycling in marine sediments: A model analysis. *Aquatic Geochemistry*, *22*(5–6), 469–504. https://doi.org/10.1007/s10498-016-9301-7

van de Velde, S., Van Lancker, V., Hidalgo-Martinez, S., Berelson, W. M., & Meysman, F. J. R. (2018). Anthropogenic disturbance keeps the coastal seafloor biogeochemistry in a transient state. *Scientific Reports*, *8*(1), 5582. https://doi.org/10.1038/s41598-018-23925-y

van de Velde, S. J., Reinhard, C. T., Ridgwell, A., & Meysman, F. J. (2020). Bistability in the redox chemistry of sediments and oceans. *Proceedings of the National Academy of Sciences of the United States of America*, *117*(52), 33043–33050. https://doi.org/10.1073/pnas.2008235117

Viollier, E., Rabouille, C., Apitz, S., Breuer, E., Chaillou, G., Dedieu, K., et al. (2003). Benthic biogeochemistry: State of the art technologies and guidelines for the future of in situ survey. *Journal of Experimental Marine Biology and Ecology*, *285*, 5–31. https://doi.org/10.1016/s0022-0981(02)00517-8

Wang, Y., & Van Cappellen, P. (1996). A multicomponent reactive transport model of early diagenesis: Application to redox cycling in coastal marine sediments. *Geochimica et Cosmochimica Acta*, *60*(16), 2993–3014. https://doi.org/10.1016/0016-7037(96)00140-8

Wijsman, J., Herman, P., Middelburg, J., & Soetaert, K. (2002). A model for early diagenetic processes in sediments of the continental shelf of the black sea. *Estuarine, Coastal and Shelf Science*, *54*(3), 403–421. https://doi.org/10.1006/ecss.2000.0655

Wu, J., Rabouille, C., Charmasson, S., Reyss, J. L., & Cagnat, X. (2018). Constraining the origin of recently deposited particles using natural radionuclides 7Be and 234Thex in deltaic sediments. *Continental Shelf Research*, *165*, 106–119. https://doi.org/10.1016/j.csr.2018.06.010

Zebracki, M., Eyrolle-Boyer, F., Evrard, O., Claval, D., Mourier, B., Gairoard, S., et al. (2015). Tracing the origin of suspended sediment in a large Mediterranean River by combining continuous river monitoring and measurement of artificial and natural radionuclides. *Science of the Total Environment*, *502*, 122–132. https://doi.org/10.1016/j.scitotenv.2014.08.082

Zhao, M., Zhang, S., Tarhan, L. G., Reinhard, C. T., & Planavsky, N. (2020). The role of calcium in regulating marine phosphorus burial and atmospheric oxygenation. *Nature Communications*, *11*(1), 1–8. https://doi.org/10.1038/s41467-020-15673-3

21699291, 2025, 6, Downloaded from https://agupubs.onlinelibrary.wiley.com/doi/10.1029/2025JC022414 by Universitetsbiblioteket, Wiley Online Library on [07/01/2026]. See the Terms and Conditions (https://onlinelibrary.wiley.com/terms-and-conditions) on Wiley Online Library for rules of use; OA articles are governed by the applicable Creative Commons License